JOURNAL OF COMPUTATIONAL PHYSICS **125,** 354–377 (1996)
ARTICLE NO. 0099

On Bi-grid Local Mode Analysis of Solution Techniques for 3-D Euler and Navier–Stokes Equations

S. O. IBRAHEEM* AND A. O. DEMUREN

Department of Mechanical Engineering, Old Dominion University, Norfolk, Virginia 23529

Received May 6, 1994; revised March 15, 1995

A procedure is presented for utilizing a bi-grid stability analysis as a practical tool for predicting multigrid performance in a range of numerical methods for solving Euler and Navier–Stokes equations. Model problems based on the convection equation, the diffusion equation, and Burger's equation are used to illustrate the superiority of the bi-grid analysis as a predictive tool for multigrid performance in comparison to the smoothing factor derived from conventional von Neumann analysis. For the Euler equations, bi-grid analysis is presented for three upwind difference based factorizations, namely spatial, eigenvalue, and combination splits, and two central difference based factorizations, namely LU and ADI methods. In the former, both the Steger–Warming and van Leer flux-vector splitting methods are considered. For the Navier–Stokes equations, only the Beam–Warming (ADI) central difference scheme is considered. In each case, estimates of multigrid convergence rates from the bi-grid analysis are compared to smoothing factors obtained from single-grid stability analysis. Effects of grid aspect ratio and flow skewness are examined. Both predictions are compared with practical multigrid convergence rates for 2-D Euler and Navier–Stokes solutions based on the Beam–Warming central difference scheme, and 3-D Euler solutions with various upwind difference schemes. It is demonstrated that bi-grid analysis can be used as a reliable tool for the prediction of practical multigrid performance.

1. INTRODUCTION

Multiple grids were first proposed in the form of two-grid level schemes to accelerate the convergence of iterative procedures by researchers such as Federenko [1]. Full multiple grid methods were later introduced by Federenko [2] to solve the Poisson equation and the approach was generalized by Bakhalov [3] to any second-order elliptic operator with continuous coefficients. According to Stuben and Trottenberg [4], Hackbush in [5] also independently developed some fundamental elements of the multigrid method. Perhaps the most influential work on the application of multigrid methods to elliptic type problems is that of Brandt [6], who also proposed the use of local mode analysis to determine the smoothing rate of multigrid schemes.

In local mode analysis, the spectral radius of a particular relaxation technique computed over only the high-frequency modes is used as a measure of the relaxation's effectiveness in a multigrid scheme since, in this case, the role of relaxation is not to reduce the total error but to smoothen it out, i.e., to remove the high-frequency components. It is assumed that the high-frequency modes have short wavelengths that are spatially decoupled and that all high-frequency waves are completely ''killed'' on the fine grid and are not visible to the coarse grids. This, however, is not always the case, since the intergrid processes also influence the convergence rate. Brandt [7] presented theoretical considerations for including the transfer processes in the local mode analysis in what is called the bi-grid method. Also, some theoretical background is given by Stuben and Trottenberg [4] on how to compute a more realistic amplification factor for multigrid methods based on the bi-grid analysis, and some convergence norms are computed for the Poisson and Helmholtz equations.

A number of works exist where the smoothing factor has been used to predict multigrid performance in practice. However, the bi-grid analysis is becoming more attractive because of its better accuracy and reliability. Van Asselt [8] used the bi-grid analysis to determine the proper amount of artificial viscosity to add at different levels of coarse grids in a multigrid application. Mulder [9, 10] has also used the bi-grid method to construct an effective semi-coarsening in a multigrid method that can solve the problem of strong alignment which often occurs in convection problems. To select a relaxation scheme for a multigrid method suitable for parallel solution of a time-dependent problem, Horton and Vandewall [11] employed this technique using the heat equation as their model problem. The cause of the poor multigrid convergence rate that is experienced in high-Reynolds-number flows, where the coarse grid corrections fail to approximate the fine grid problem well enough for certain components, has also been investigated by Brandt and Yavneh [12] using the bi-grid method. In an effort to develop an effective multigrid algorithm for Navier–Stokes solutions on an unstructured grid with $O(N)$ complexity,

* Now with The Pennsylvania State University.

0021-9991/96 $18.00

Morano [13] and Morano and Dervieux [14] have used the bi-grid analysis on a 1-D model scalar convection equation with periodic boundary conditions. More recently, Ibraheem and Demuren [15] also presented some convergence norms for Burger's equation based on bi-grid analysis.

Implicit numerical schemes are becoming very popular, since they allow large time steps in advancing the solution of Euler and Navier–Stokes equations to steady state. However, only a few works exist to show the effectiveness of multigrid methods, especially when approximate factorization is introduced. Jameson and Yoon [16] and Caughey [17], for example, used the smoothing factor and scalar convection equation as a model for the Euler equations to investigate multigrid performance. Anderson *et al.* [18] and Demuren and Ibraheem [19] have also computed the smoothing factors on the actual coupled Euler equations for some popular approximate factorizations. The latter work investigated the Navier–Stokes equations as well.

The objective of the present work is to present a procedure for utilizing the bi-grid amplification factor as a more reliable practical tool for predicting multigrid performance in a range of numerical methods. Bi-grid analysis, based on the von Neumann type method, is first presented for 1-D convection and diffusion model problems and the linearized Burger's equation. Numerical results from practical multigrid solutions of these problems are compared to both predictions from bi-grid analysis and smoothing factors derived from the more usual single grid analysis. Both analyses and practical computations are based on the following different time-stepping methods: an Euler forward explicit scheme, a Runge–Kutta multistage scheme, a fully implicit scheme, and the semi-implicit scheme. The influence of the Peclet number on the convergence characteristics of the different schemes is investigated using Burger's equation. Finally, for more practical situations, multigrid performance of various approximate factorizations for the 3-D Euler and Navier–Stokes equations is examined using the bi-grid stability analysis. For the Euler equations, bi-grid analysis is presented for three upwind difference-based factorizations and several central difference-based factorizations. In the upwind factorizations, the flux-vector splitting methods of Steger and Warming and of van Leer are considered. The central schemes include the Lower and Upper (LU) and ADI factorizations. The time-stepping algorithm for the Navier–Stokes equations is based on the Beam–Warming central difference scheme only. Practical multigrid solutions from a numerical experiment on the ADI method are also compared to both predictions from bi-grid analysis and smoothing factors.

2. BI-GRID ANALYSIS

Consider a given differential problem which can be written as

$$L\{u(x)\} = f(x) \quad \text{for } x \text{ in } \Omega, \tag{1}$$

where L is a linear operator. A typical 2-level multigrid cycle solution to this problem will involve the following steps:

(1) pre-relaxation on a fine grid using any technique S_1, ν^1 times

(2) computation of the defect R

(3) restriction of the defect to the coarser grid

(4) exact solution of the error equation on the coarse grid

(5) prolongation of the error onto and the correction on the fine grid

(6) post-relaxation on the fine grid using any technique S_2, ν^2 times.

These can be represented for any intermediate solution w by using the usual operators as follows:

$$\begin{aligned}
&(1)\ w^{n+1/2} = S_1^{\nu^1} w^n \\
&(2)\ R = f - L_h w^{n+1/2} \\
&(3)\ I_h^H R \\
&(4)\ \nu_H = L_H^{-1}(I_h^H R) \\
&(5)\ I_H^h \nu_H + w^{n+1/2} \\
&(6)\ w^{n+1} = S_2^{\nu^2}(I_H^h \nu_H + w^{n+1/2}).
\end{aligned} \tag{2}$$

Combining these steps, we can write

$$w^{n+1} = S_2^{\nu^2}[I_H^h L_H^{-1} I_h^H (f - L_h S_1^{\nu^1} w^n) + S_1^{\nu^1} w^n]. \tag{3}$$

The steady-state solution (u) is not changed by the coarse grid correction scheme; thus

$$u^{n+1} = S_2^{\nu^2}[I_H^h L_H^{-1} I_h^H (f - L_h S_1^{\nu^1} u^n) + S_1^{\nu^1} u^n]. \tag{4}$$

Subtracting (2) from (1) and noting that $e^{n+1} = u^{n+1} - w^{n+1}$ gives

$$\begin{aligned}
e^{n+1} &= S_2^{\nu^2}(I - I_H^h L_H^{-1} I_h^H L_h) S_1^{\nu^1} e^n \\
&= S_2^{\nu^2} K S_1^{\nu^1} e^n \\
&= M e^n,
\end{aligned} \tag{5}$$

where

$$\begin{aligned}
K &= I - I_H^h L_H^{-1} I_h^H L_h \\
M &= S_2^{\nu^2}(I - I_H^h L_H^{-1} I_h^H L_h) S_1^{\nu^1}.
\end{aligned} \tag{6}$$

Here M is the bi-grid amplification matrix and K is the coarse grid correction matrix. It can be shown [4] that when linear operators are used for the restriction, I_h^H, and the prolongation, I_H^h, transfer processes, the coarse grid correction matrix is not a convergent iteration matrix; i.e.,

$$\varrho(K) = \varrho(I - I_H^h L_H^{-1} I_h^H L_h) \geq 1. \tag{7}$$

Hence, the fine grid smoothing steps, S_1 and S_2, are important for a convergent scheme. The spectral radius of the bi-grid amplification matrix ($\lambda_{\max\_bg}$) and its l_2 norm can be used to predict the performance of a multigrid method. While the spectral radius measures the asymptotic convergence rate of the multigrid method, the l_2 norm measures the actual error reduction per iteration. $\lambda_{\max\_bg}$ is defined as follows:

$$\lambda_{\max\_bg} = \max\{\varrho[\hat{M}(\Theta)]\}. \tag{8}$$

Here $\hat{M}(\Theta)$ is the Fourier representation of the matrix M. A brief comment about Θ will be in order. Due to the aliasing process, low-frequency modes will couple with the coarse grid Fourier modes and, thus, for any $\Theta^1 = \{\theta_x, \theta_y, \theta_z\}$ such that $-\pi/2 \leq \theta_x, \theta_y, \theta_z \leq \pi/2$, there exists a corresponding set of harmonics up to an integer multiple of 2π. For $1-$D, $2-$D, and $3-$D problems, we define Θ as the following set:

$$\begin{aligned}
1-\mathrm{D}\ \Theta &= \{(\theta_x), (\theta_x \pm \pi)\} \\
2-\mathrm{D}\ \Theta &= \{(\theta_x, \theta_y), (\theta_x, \theta_y \pm \pi), (\theta_x \pm \pi, \theta_y), \\
&\qquad (\theta_x \pm \pi, \theta_y \pm \pi)\} \\
3-\mathrm{D}\ \Theta &= \{(\theta_x, \theta_y, \theta_z), (\theta_x, \theta_y, \theta_z \pm \pi), (\theta_x, \theta_y \pm \pi, \theta_z), \\
&\qquad (\theta_x, \theta_y \pm \pi, \theta_z \pm \pi), \\
&\qquad (\theta_x \pm \pi, \theta_y, \theta_z), (\theta_x \pm \pi, \theta_y, \theta_z \pm \pi), \\
&\qquad (\theta_x \pm \pi, \theta_y \pm \pi, \theta_z), \\
&\qquad (\theta_x \pm \pi, \theta_y \pm \pi, \theta_z \pm \pi)\}.
\end{aligned} \tag{9}$$

Or more generally,

$$d-\mathrm{D}\ \Theta = \{\Theta^1, \Theta^2, \Theta^3, ..., \Theta^{2^d}\} \tag{10}$$

(where d is the dimensionality of the space, and Θ^1, Θ^2, ..., Θ^{2d} are permuted in a similar manner with the $\pm$ signs chosen so that the harmonics lie in the high-frequency range).

Hence, based on the Θ components and on the number of degrees of freedom of the problem, q, $\hat{M}(\Theta)$ is a $2^d q \times 2^d q$ matrix. Thus, it is a 2×2 matrix for a $1-$D scalar problem and a 40×40 matrix for the Euler or Navier–Stokes equations in $3-$D. The Fourier representation for the corresponding operators, smoothing factor, fine grid problem, interpolation, restriction, and the coarse grid problem, can be constructed as follows [7]:

$$\begin{aligned}
\hat{S} &= (\hat{S}_2^{\nu^2}, \hat{S}_1^{\nu^1}) = \mathrm{diag}[\hat{S}(\Theta^1), \hat{S}(\Theta^2), ..., \hat{S}(\Theta^{2^d})] && 2^d q \times 2^d q \\
\hat{L}_h &= \mathrm{diag}[\hat{L}(\Theta^1), \hat{L}(\Theta^2), ..., \hat{L}(\Theta^{2^d})] && 2^d q \times 2^d q \\
\hat{I}_H^h &= [\hat{I}_H^h(\Theta^1), \hat{I}_H^h(\Theta^2), ..., \hat{I}_H^h(\Theta^{2^d})] && 2^d q \times q \\
\hat{I}_h^H &= [\hat{I}_h^H(\Theta^1), \hat{I}_h^H(\Theta^2), ..., \hat{I}_h^H(\Theta^{2^d})] && q \times 2^d q \\
\hat{L}_H &= \hat{L}(2\Theta^1) && q \times q.
\end{aligned} \tag{11}$$

The difference operator, $\hat{L}_H(2\Theta^1)$, on the coarse grid is only $q \times q$ since the coarse grid problem is solved exactly.

$\hat{S}$ and $\hat{L}$ depend on the choice of the smoother and the governing equations, respectively. The transfer processes, however, are less problem-dependent. Following [7], the Fourier symbol of the prolongation operator based on an Ith-order polynomial is given by

$$\hat{I}_H^h(\Theta^m)_{kl} = \delta_{kl} \prod_{i=1}^{d} \psi_I(\cos \Theta_i^m) \quad m = 1, 2^d, \tag{12}$$

where $\psi_2(\xi) = (1 + \xi)/2$, $\psi_4(\xi) = (2 + 3\xi - \xi^2)/4$, etc., are the 2nd and 4th order interpolation functions, and δ_{kl} is the Kronecker delta. We restrict our analysis to the 2nd order since it is more commonly used. The restriction operator is expressed as

$$2^d \hat{I}_h^H(\Theta^m) = [\hat{I}_H^h(\Theta^m)]^{\mathrm{T}^*}. \tag{13}$$

T* in the above equation represents the conjugate transpose. The restriction operator is often the adjoint of the prolongation operator in practice. In this study, the corresponding full weighting is used for the restriction operation for the Euler and Navier–Stokes equations, while simple injection is employed for the model problems. In the latter case, the Fourier symbol for the restriction operator is simply unity.

A description of how the Fourier representation $\hat{M}(\Theta)$ can be constructed is given later for certain problems.

3. MODEL EQUATIONS

The model equations used in the present study are the conservation equations for the convection of a scalar, the diffusion of a scalar, and the linearized Burger's equation which is essentially a convection–diffusion equation. Each of these equations is integrated in time using (i) an Euler forward-explicit scheme, (ii) a Runge–Kutta multistage scheme, (iii) a fully implicit scheme, and (iv) a semi-implicit scheme.

The model equations for convection, diffusion, and the linear Burger's equation can be written as

$$\begin{aligned} &\text{convection: } u_t + cu_x = 0 \\ &\text{diffusion: } \; u_t - \nu u_{xx} = 0 \\ &\text{(convection–diffusion) Burger's: } u_t^* + u_0 u_x^* = \nu u_{xx}^*. \end{aligned} \tag{14}$$

In the Burger's equation, u_0 = constant is assumed in our analysis. Thus, it can be put in the non-dimensional form

$$u_t + u_x = \frac{1}{\mathrm{Pe}} u_{xx}, \tag{15}$$

where Pe in the above equation is the Peclet number, defined as follows:

$$\mathrm{Pe} = \frac{u_0 D}{\nu} \tag{16}$$

(D is an appropriate length scale).

(i) *Euler Forward-Explicit Scheme.* The Euler explicit method can be applied to the above equations to yield the general discrete form

$$u_i^{n+1} = u_i^n - \Delta t R^n, \tag{17}$$

where R^n represents the residual expressed as follows:

$$\begin{aligned} &\text{convection: } R^n = \frac{c}{\Delta x}(u_i^n - u_{i-1}^n) \\ &\text{diffusion: } \quad R^n = -\frac{\nu}{\Delta x^2}(u_{i+1}^n - 2u_i^n + u_{i-1}^n) \\ &\text{Burger's: } \quad R^n = \frac{1}{\Delta x}(u_i^n - u_{i-1}^n) - \frac{1}{\Delta x^2 \mathrm{Pe}} \\ &\qquad\qquad (u_{i+1}^n - 2u_i^n + u_{i-1}^n). \end{aligned} \tag{18}$$

Space discretization in the above formulations is based on first-order upwind differences for convection, second-order central differences for diffusion, and the corresponding combination in Burger's equation. First-order upwind differencing of the convective flux introduces inaccuracy due to too much numerical diffusion, which may be of the same order as the natural diffusion in Burger's equation. If second-order central differencing is used for the convective flux, a second-order accurate scheme can be obtained but with severe limitations on the Peclet number due to dispersion errors. Although the addition of artificial viscosity could dampen the high-frequency oscillations at high Peclet numbers, it is highly problem dependent. A better approach to achieve second-order accuracy while sustaining a smooth solution at the vicinity of shock or high gradients is to discretize the convective flux using higher-order upwind schemes, preferably in conjunction with some limiter. Hence, with a third-order discretization of the convective flux, a second-order accurate scheme for Burger's equation can be obtained with R^n given by

$$\begin{aligned} R^n = &\frac{1}{2\,\Delta x}(u_{i+1}^n - u_{i-1}^n) - \frac{1}{6\,\Delta x}(u_{i+1}^n - 3u_i^n + 3u_{i-1}^n - u_{i-2}^n) \\ &- \frac{1}{\Delta x^2 \mathrm{Pe}}(u_{i+1}^n - 2u_i^n + u_{i-1}^n). \end{aligned} \tag{19}$$

(ii) *Runge–Kutta Multistage Scheme.* With each of the above schemes integrated in time using the Euler forward explicit method, the time step was limited to a small range by stability considerations, thus making it inefficient for steady-state computations. A Runge–Kutta (RK) method was introduced by Jameson *et al.* [20] to permit larger time steps to be taken. For an m-stage scheme, the time integration can be written as follows:

$$\begin{aligned} u_i^0 &= u_i^n \\ u_i^k &= u_i^0 - \alpha_k \Delta t R^{k-1} \quad k = 1, m \\ u_i^{n+1} &= u_i^m. \end{aligned} \tag{20}$$

Note that with $m = 1$, the RK scheme reduces to the Euler forward explicit scheme and hence is sometime called RK1. Coefficients α_k are optimized such that larger time steps can be used for faster convergence.

Three different sets of coefficients for a 4-stage Runge–Kutta scheme are investigated in this study, in line with the earlier work of Morano [13]. These are the standard coefficients (RK4-S, $\alpha_1 = 0.25$, $\alpha_2 = 0.3333$, $\alpha_3 = 0.5$, $\alpha_4 = 1$), and the optimized coefficients of Lallemand (RK4-L, $\alpha_1 = 0.11$, $\alpha_2 = 0.2766$, $\alpha_3 = 0.5$, $\alpha_4 = 1$) and van Leer (RK4-VL, $\alpha_1 = 0.0833$, $\alpha_2 = 0.2069$, $\alpha_3 = 0.4265$, $\alpha_4 = 1$).

(iii) *Implicit Scheme.* An implicit time integration scheme can easily be formulated for each of our model problems. For example, the corresponding implicit formulation for Burger's equation with first-order accuracy is written in delta form as follows:

$$\begin{aligned} &\left[-\beta\left(\frac{\Delta t}{\Delta x} + \frac{\Delta t}{\mathrm{Pe}\,\Delta x^2}\right)\right]\Delta u_{i-1}^n + \left[1 + \beta\left(\frac{\Delta t}{\Delta x} + \frac{2\,\Delta t}{\mathrm{Pe}\,\Delta x^2}\right)\right] \\ &\qquad \Delta u_i^n - \beta\left(\frac{\Delta t}{\mathrm{Pe}\,\Delta x^2}\right)\Delta u_{i+1}^n = -\Delta t R^n \\ &R^n = \frac{1}{\Delta x}(u_i^n - u_{i-1}^n) - \frac{1}{\Delta x^2 \mathrm{Pe}}(u_{i+1}^n - 2u_i^n + u_{i-1}^n) \\ &\qquad \Delta u_i^n = u_i^{n+1} - u_i^n. \end{aligned} \tag{21}$$

β in the above formulation is called the implicitness factor; $\beta = 1.0$ gives a fully implicit scheme.

(iv) *Semi-Implicit Scheme.* If $\beta = 0.5$ in Eq. (21) above we have a semi-implicit scheme. This reduces to the Crank–Nicolson scheme if the overall spatial differencing is second-order accurate.

Fourier Symbols

For illustration, the bi-grid amplification marix $\hat{M}(\Theta)$ is constructed for the convection problem using the Euler-forward explicit scheme for the smoother.

Consider the discrete form of the operator L and let the step-by-step solution be characterized by Fourier modes (with periodic boundary conditions)

$$u^n = U_0 \lambda^n e^{\theta_x Ii}. \tag{22}$$

Then each of the operators that forms matrix $\hat{M}(\Theta)$ becomes

$$\begin{aligned}
\hat{S}(\Theta^m) &= \left(1 - \frac{c\,\Delta t}{\Delta x}\right) + \frac{c\,\Delta t}{\Delta x}[\cos(\Theta^m) - I\sin(\Theta^m)] \\
\hat{L}_h(\Theta^m) &= -\frac{1}{\Delta x}[1 - \cos(\Theta^m) + I\sin(\Theta^m)] \\
\hat{I}_H^h(\Theta^m) &= \tfrac{1}{2}[1 + \cos(\Theta^m)] \quad m = 1, 2 \\
\hat{I}_h^H(\Theta^m) &= 1 \quad \text{for injection} \\
\hat{L}_H &= -\frac{1}{2\,\Delta x}[1 - \cos(2\Theta^1) + I\sin(2\Theta^1)]
\end{aligned} \tag{23}$$

where

$$\Theta^1 = \theta_x \quad \text{and} \quad \Theta^2 = \theta_x + \pi.$$

Thus, from Eq. (8), $\hat{M}(\Theta)$ can be written

$$\hat{M}(\Theta) = \begin{bmatrix} \hat{S}(\Theta^1) & 0 \\ 0 & \hat{S}(\Theta)^2) \end{bmatrix}^{\nu_1} \begin{bmatrix} K_{11} & K_{12} \\ K_{21} & K_{22} \end{bmatrix} \begin{bmatrix} \hat{S}(\Theta^1) & 0 \\ 0 & \hat{S}(\Theta^2) \end{bmatrix}^{\nu_2}$$

$$\begin{aligned}
K_{11} &= 1 - \hat{I}_H^h(\Theta^1)\hat{I}_h^H(\Theta^1)\hat{L}_h(\Theta^1)/\hat{L}_H \\
K_{12} &= -\hat{I}_H^h(\Theta^1)\hat{I}_h^H(\Theta^2)\hat{L}_h(\Theta^2)/\hat{L}_H \\
K_{21} &= -\hat{I}_H^h(\Theta^2)\hat{I}_h^H(\Theta^1)\hat{L}_h(\Theta^1)/\hat{L}_H \\
K_{22} &= 1 - \hat{I}_H^h(\Theta^2)\hat{I}_h^H(\Theta^2)\hat{L}_H(\Theta^2)/\hat{L}_H.
\end{aligned} \tag{24}$$

Note that $\hat{L}_H$ is evaluated only at the fundamental frequency; hence it is 1×1. The result obtained above is similar to that derived by Morano [13], although our presentation is more general and is more easily extended to multiple dimensions.

Multigrid Implementation

A simple two-level multigrid (V cycle) method was implemented to test the relative accuracy of the bi-grid amplification factor and the smoothing factor in predicting multigrid performance. The two-level algorithm consists of the steps given in Section 2 and is recursively expressible as follows:

```
Proc Multigrid (u^n, u^{n+1}, R^n, k)
    {if (k = 1)
        either  u^{n+1} = L_H^{-1} R^n
        or      u^{n+1} = S^∞ u^n
    else
        u^{n+1} ← S^1 u^n
        R^n ← I_h^H (R^n − L u^n)
        Multigrid (0, u_H, R^n, k − 1)
        u^{n+1} ← u^{n+1} + I_H^h u_H
    endif}
```
(25)

In the above, L and S stand, respectively, for the discrete operator and relaxation scheme corresponding to each of the model equations and numerical schemes discussed in previous sections. For this two-level V cycle multigrid implementation, only one pre-relaxation with no post-relaxation is performed on the fine grid. The residual equation on the coarse grid is solved exactly, using as many iterations as necessary. This ensures consistency with the bi-grid analysis in Section 2. It also enables the two-level scheme to simulate more closely the performance of true multigrid schemes which would be expected to have several grid levels. In the latter, the coarse grid residual problem is solved more efficiently through recursive application of the basic two-level algorithm and the residual problem is only solved exactly on the coarsest grid. Thus, the present two-level scheme gives a good estimate of the practical multigrid convergence rate, based on the number of fine grid iterations, even for cases in which several grid levels are utilized.

Local Relaxation

Bi-grid analysis is exact for problems with periodic boundary conditions since it is based on the Fourier method. However, the asymptotic convergence rate for certain multigrid solutions deteriorates from the bi-grid prediction due to singularities such as discontinuity in material and/or solutions, and also due to the type and coefficients of the boundary conditions. Poor multigrid performance results since such singularities lead to too large a correction from the coarse grids in the localized region. To improve the performance of a multigrid solution, further relaxation can be performed on the fine grid in the region of the singularities after applying the coarse grid correction. This local relaxation is, in fact, an extra post-relax-

ation but confined to only certain nodal points and carried out a few times. The extra computational work is negligible if only a few partial sweeps are involved. The convection dominated problems subject to Dirichlet boundary conditions that are considered here undergo high changes in gradient in order to satisfy the exit boundary conditions. Therefore, multigrid performance in these problems deviates from the results predicted by bi-grid. However, a few passes on the fine grid over the boundary conditions and over the interior equation in some small neighborhood of the boundary (about three nodal points at the exit) is found sufficient to improve multigrid performance to the exact value predicted by bi-grid analysis.

Numerical Experiments

The bi-grid amplification factor ($\lambda_{\max\_bg}$), the smoothing factor (λ_{μ_sg}), and the practical asymptotic convergence rate (ρ_{mg}) of the multigrid scheme were obtained for the following test problems:

(1) Convection problem with periodic boundary conditions, viz.:

$$u(0, t) = u(1, t); \quad u(x, 0) = \sin 2\pi x. \quad (26)$$

(2) Convection problem with Dirichlet boundary conditions, viz.:

$$u(0, t) = 1, u(1, t) = 0 \text{ for } t > 0; u(x, 0) = \sin 2\pi x. \quad (27)$$

(3) Diffusion problem with Dirichlet boundary conditions similar to those in (2) above

(4) Burger's equation with Dirichlet boundary conditions similar to those in (2) above.

The bi-gird amplification factor is obtained from Eq. (8) and the smoothing factor is obtained from the usual single grid amplification factor over the high frequency range $\pi/2 \le \Theta^1 \le \pi$ as $\lambda_{\mu\_sg} = \max\{\rho[S(\Theta^1)]\}$. In each case, 16 Fourier modes are selected and the associated eigenvalues are solved for , using linear algebra routines such as found in the IMSL library. The asymptotic convergence rate of the multigrid experiments, on the other hand, is computed from

$$\rho_{mg} = \left(\frac{\|R^{n2}\|}{\|R^{n1}\|}\right)^{1/(n2-n1)} \quad (28)$$

where $\|R^{n1}\|$ and $\|R^{n2}\|$ are the l_2 norms of the residuals at time levels $n1$ and $n2$, respectively.

The pseudotime Δt to advance the convection and the diffusion problems to steady state is computed from CFL = $\Delta t/\Delta x$ and $d = \Delta t/\text{Pe}\ \Delta x^2$, respectively. CFL is the Courant–Friedrichs–Lewy number and d is the diffusion number. For Burger's equation, Δt is computed from

$$\Delta t = \min(\sigma\ \Delta x, \sigma\ \Delta x^2 \text{Pe}), \quad (29)$$

where σ is a parameter chosen to reduce to the diffusion number d at low Pe number and to the CFL number at high Pe number. This choice ensures that the appropriate time step is used in each flow regime. Δx is computed from $D/(N-1)$, where N is the total number of grid points. In most of the model test problems N equaled 21, but was increased to 101 for the Burger's equation at high Peclet numbers, in order to reproduce the exact solution more accurately. For all the model problems presented here, we obtained truly grid-independent multigrid convergence rates, so that the convergence curves in Figs. 1 to 12 would be the same irrespective of the value of N.

The exact steady-state solution for Burger's equation, subject to the boundary condition type discussed above, is given by

$$u = u(0)\left[\frac{1 - \exp[\text{Pe}\ (x/D - 1)]}{1 - \exp(-\text{Pe})}\right]. \quad (30)$$

It is valid for the whole range of Pe considered in this study.

Results for the Model Equations

Figures 1 and 2 show results of the analyses of the 1-D convection equation using the Euler forward explicit scheme. The model problem of Fig. 1 has periodic boundary conditions whereas that of Fig. 2 had Dirichlet boundary conditions. The bi-grid analysis gives perfect prediction of practical multigrid performance in the former, whereas the smoothing factors from the single grid analysis are much too high. Both methods of analysis ignore boundary effects, so the same predictions are obtained in Figs. 1 and 2, and the analyses predictions are strictly correct only for problems with periodic boundary conditions. This is confirmed in Fig. 2b, where the asympotic multigrid convergence rate is now much worse than predicted by the bi-grid analysis. The reason for the degradation of the multigrid performance is the singularity which appears near the exit in Fig. 2a. This degradation in performance could be cured with a few local relaxation sweeps [7], as shown in Fig. 2c. Each sweep had marginal computational cost and five sweeps were sufficient to bring the multigrid performance for the Dirichlet problem in line with that with periodic boundary conditions and the prediction of the bi-grid analysis. Clearly the Euler forward explicit scheme does not have good convergence properties except for CFL numbers close to 0.5, and it is divergent for CFL numbers greater than 1. Better convergence properties are achieved with Runge–Kutta (RK) schemes. Three four-

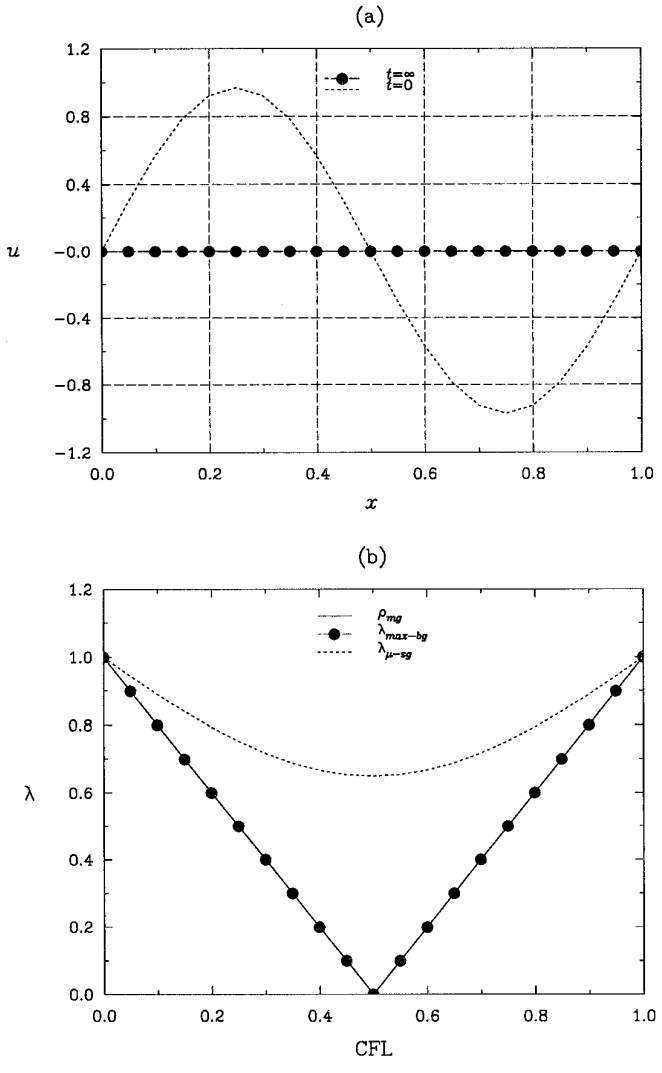

FIG. 1. 1-D convection equation: (a) steady solution; (b) convergence characteristics (Euler forward explicit; periodic B,C.'s).

stage RK schemes were analyzed, and the results are shown in Fig. 3 for the 1-D convection problem with periodic boundary conditions. With optimized coefficients, Fig. 3c, convergence could be obtained for CFL numbers up to 3. Further, bi-grid amplification factors below 0.4 are obtained for the range of CFL numbers from 0.5 to 2.5. There is also perfect agreement between the results of the bi-grid analysis and the practical multigrid convergence rates. Similar multigrid results were obtained by Morano [13]. Figure 4 shows the result for the Dirichlet boundary conditions. In this case the multigrid convergence rates at higher CFL numbers are much better than predicted by either method. Clearly, the boundary effects are stronger with the RK scheme and there is no simple way to account for them in the analyses. Figure 5 shows results for a fully implicit scheme and for the semi-implicit Crank–Nicolson scheme, for the 1-D convection equation. Although both schemes are stable for the whole range of CFL numbers, the Crank–Nicolson scheme suffers from very poor convergence rate at high CFL numbers.

Results of the 1-D diffusion equation are presented in Figs. 6–8. Dirichlet boundary conditions are applied throughout, and the steady state solution is shown in Fig. 6a. In each case, the bi-grid analysis gives perfect agreement with the multigrid convergence rate whereas the smoothing rate obtained from the single grid analysis is consistently too optimistic. On the whole, the predicted convergence rates for each method are similar to corresponding ones obtained from the convection equation if the diffusion number d is replaced by the CFL number in the latter. Clearly, if the goal is to achieve rapid convergence to the steady state, the fully implicit scheme with high d or CFL number is the obvious choice. Implicit schemes are, of course, computationally more expensive since they require matrix inversion or iterative solution.

The linearized Burger's equation represents a mixed convection–diffusion problem. The whole range of model types from pure diffusion to pure convection can be obained simply by varying the Peclet number from a very small value to a very large value. Computed results for four values of Pe (10^{-4}, 20, 100, 10^6) are presented in Figs. 9–12, for the various discretization schemes considered here. The exact solution at the steady state is shown in Fig. 9a, for the Dirichlet boundary conditions $u(0, t) = 1$, $u(1, t) = 0$. For high values of Pe, there is a singularity near $x = 1$. As explained previously, local relaxation is performed to reduce the adverse effect of this singularity on the overall multigrid convergence rate. The results for the first- and second-order Euler time explicit schemes are presented in Figs. 9 and 10. In each case the bi-grid analysis gives a quite good prediction of the multigrid convergence rate. On the other hand, single-grid analysis gives too optimistic estimates at low Pe and too pessimistic estimates at high Pe. The second-order scheme shows much poorer convergence rates, especially at high Pe. The results for the fully implicit and semi-implicit schemes are presented in Figs. 11 and 12. The superiority of the fully implicit scheme is confirmed, especially for high Pe flows. For σ (or CFL number) greater than 10, it is close to a direct solver with $\lambda \to 0$. In these cases, too, the bi-grid analysis agrees quite well with the practical multigrid convergence rate, except near $\sigma = 1$ in the semi-implicit scheme at high Pe. Because of the limited range of σ where the convergence rate is much less than 1, the semi-implicit Crank–Nicolson scheme is not a viable method for obtaining steady solutions for the model problem. If the main interest in these 1-D problems is rapid convergence to steady state, then the fully implicit scheme at high values of σ (or CFL number) will be optimal. However, in multidimensional problems, the overheads associated with the required ma-

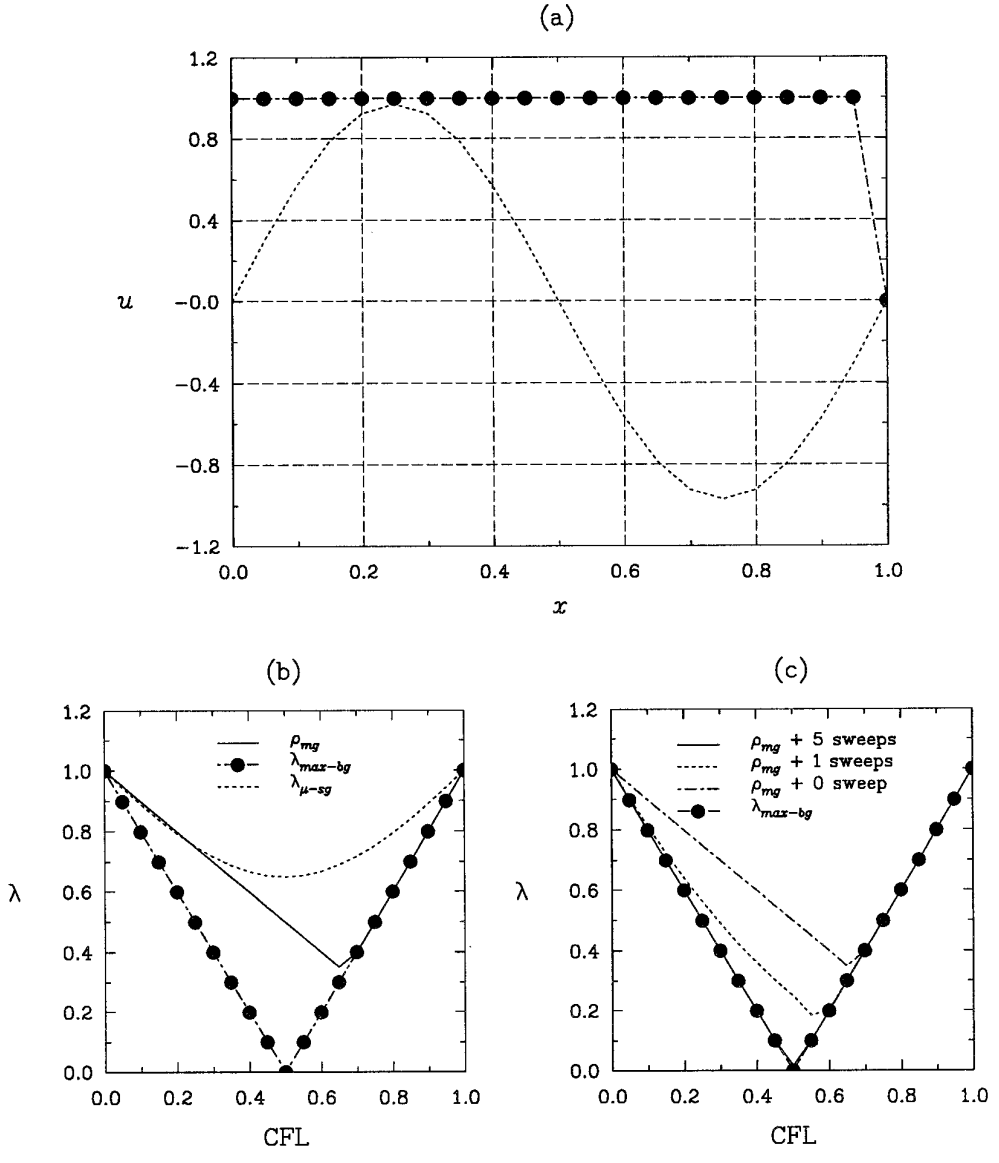

FIG. 2. 1-D convection equation; (a) steady solution; (b) convergence characteristics without local relaxation; (c) convergence characteristics with local relaxation (Euler forward explicit; Dirichlet B.C.'s).

trix inversions are so high that the exact implementation of the fully implicit scheme is not practical. Thus approximate methods such as are discussed in Section 4 must be used, with corresponding degradation in convergence rate.

Thus far, bi-grid stability analysis has been presented for typical explicit and implicit solution methods for model problems which range from the diffusion equation to the convection equation and including the convection–diffusion equation at different Peclet numbers. For large scale practical computations, interest is really in solving the system of Euler or Navier–Stokes equations in multiple dimensions. In the following section, the bi-grid stability analysis of fully implicit schemes which use various approximate factorization methods to solve the Euler and Navier–Stokes equations are examined.

4. EULER AND NAVIER-STOKES EQUATIONS

In order to extend the bi-grid analysis to the coupled equations of fluid flows, a discrete analog of these equations is formulated based on different approximate factorizations. The ADI factorization is formulated for the Navier–Stokes equations with the Euler equations as a degenerate case. Three different upwind factorizations and one central LU factorization formulated in [19] are, also, considered.

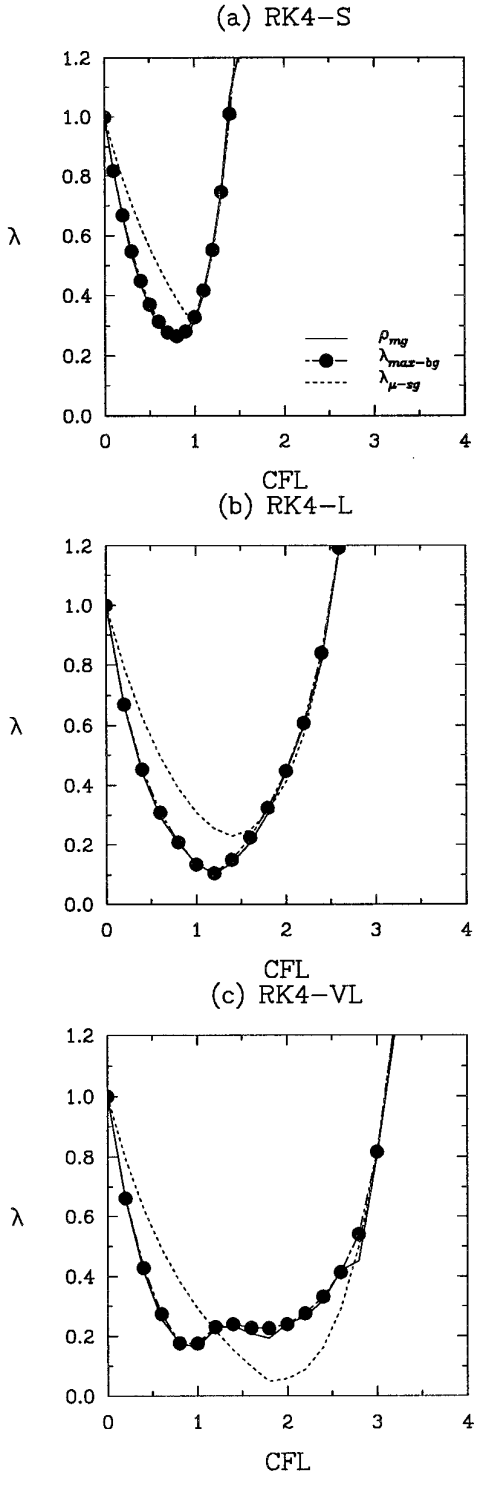

FIG. 3. Convergence characteristics for 1-D convection equation: (a) standard (b) Lallemand; (c) van Leer coefficients (4-stage Runge–Kutta; Periodic B.C.'s).

The 3-D Navier–Stokes equations in Cartesian coordinates can be written as

$$\frac{\partial Q}{\partial t} + \frac{\partial (E - E_v)}{\partial x} + \frac{\partial (F - F_v)}{\partial y} + \frac{\partial (G - G_v)}{\partial z} = 0, \quad (31)$$

where Q is the solution vector and E, F, G are the conserved inviscid fluxes:

$$\begin{aligned} Q &= [\rho, \rho u, \rho v, \rho w, \rho e]^{\mathrm{T}} \\ E &= [\rho u, \rho u^2 + p, \rho uv, \rho uw, (\rho e + p)u]^{\mathrm{T}} \\ F &= [\rho v, \rho vu, \rho v^2 + p, \rho vw, (\rho e + p)v]^{\mathrm{T}} \\ G &= [\rho w, \rho wu, \rho wv, \rho w^2 + p, (\rho e + p)w]^{\mathrm{T}}. \end{aligned} \quad (32)$$

This viscous fluxes E_v, F_v, G_v are

$$\begin{aligned} E_v &= [0, \tfrac{2}{3}\mu(2u_x - v_y - w_z), \mu(u_y + v_x), \mu(u_z + w_x), \\ &\quad \mu v(u_y + v_x) + \mu w(u_z + w_x) + \tfrac{2}{3}\mu u(2ux - v_y - w_z) + kT_x]^{\mathrm{T}} \\ F_v &= [0, \mu(u_y + v_x), \tfrac{2}{3}\mu(2v_y - u_x - w_z), \mu(v_z + w_y), \\ &\quad \mu u(u_y + v_x) + \mu w(v_z + w_y) + \tfrac{2}{3}\mu v(2v_y - u_x - w_z) + kT_y]^{\mathrm{T}} \\ G_v &= [0, \mu(w_x + u_z), \mu(v_z + w_y), \tfrac{2}{3}\mu(2w_z - v_y - u_x), \\ &\quad \mu u(w_x + u_z) + \mu v(v_z + w_y) + \tfrac{2}{3}\mu w(2w_z - v_y - u_x) + kT_z]^{\mathrm{T}}. \end{aligned} \quad (33)$$

In the above, $T = p/[\rho c_v(\gamma - 1)]$, and $p = (\gamma - 1)[\rho e - 0.5(u^2 - v^2 + w^2)]$. Also, the Stokes hypothesis ($\lambda = -\frac{2}{3}\mu$) has been assumed. With E_v, F_v, G_v set to zero, we recover the Euler equations.

Using the Beam–Warming scheme, the viscous fluxes are split directionally [21]. Following the approach presented in Anderson *et al.* [22] for 2-D Navier–Stokes equations, analysis yields the following ADI approximate factorization for 3-D Navier–Stokes equations. Here, Euler time integration and constant fluid properties are assumed:

$$\begin{aligned} &[\mathbf{I} + \Delta t(\delta_x A - \delta_{xx} R)][\mathbf{I} + \Delta t(\delta_y B - \delta_{yy} S)][\mathbf{I} \\ &\quad + \Delta t(\delta_z C - \delta_{zz} Y)]\Delta Q = -\Delta t[A\delta_x - R\delta_{xx} - R_1\delta_{yx} \\ &\quad - R_2\delta_{zx} + B\delta_y - S_1\delta_{xy} - S\delta_{yy} - S_2\delta_{zy} + C\delta_z \\ &\quad - Y_1\delta_{xz} - Y_2\delta_{yz} - Y\delta_{zz}]Q. \end{aligned} \quad (34)$$

Here the Jacobians A, B, C are $\partial E/\partial Q$, $\partial F/\partial Q$, $\partial G/\partial Q$, respectively. The analytical expression for the viscous fluxes are given in Demuren and Ibraheem [19]. The right-hand side resulted from linearization and from assuming the flux Jacobians to be locally constant. To damp the high-frequency waves that will arise due to central differencing, second-order implicit ($D_x^i = -\varepsilon_i \Delta t\ \Delta x\ \delta_{xx}$) and fourth-order explicit ($D_x^e = -\varepsilon_e\, \Delta t\, \Delta x^3\, \delta_{xxxx}$) artificial dissipations are added as diagonal matrix coefficients in the numerical

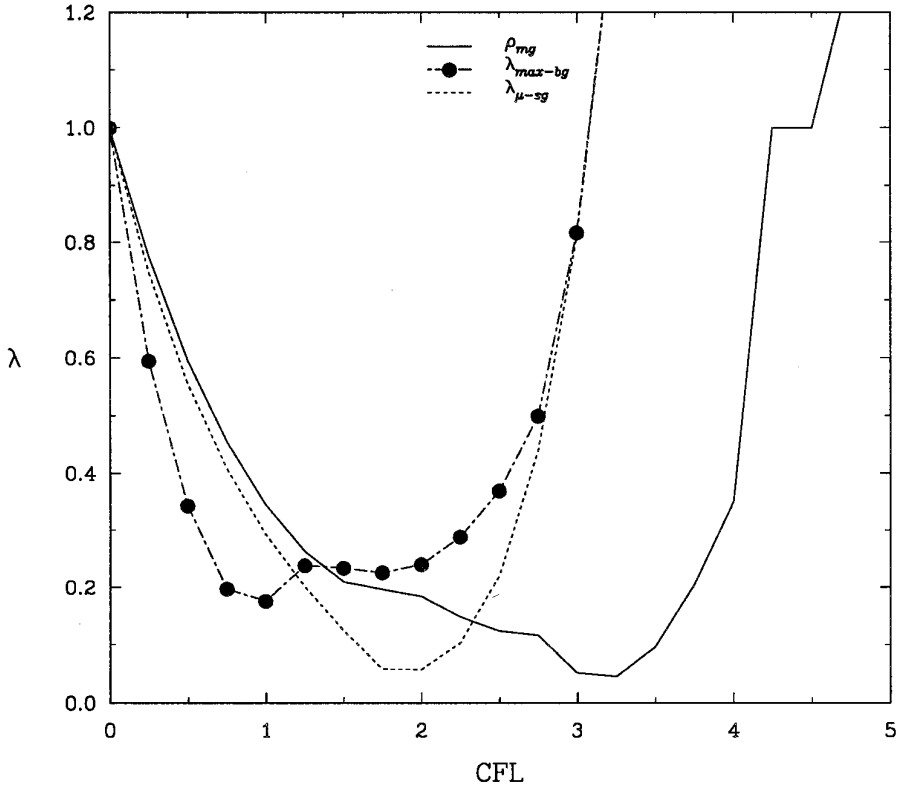

FIG. 4. Convergence characteristics for 1-D convection equation: (4-stage Runge–Kutta; Dirichlet B.C.'s; van Leer coefficients).

examples. Thus, with similar dissipations added in the y and z directions, Eq. (34) becomes

$$\begin{aligned}[\mathbf{I} + \Delta t(\delta_x A - \delta_{xx} R - \varepsilon_i \Delta x \delta_{xx})][\mathbf{I} + \Delta t(\delta_y B - \delta_{yy} S \\ - \varepsilon_i \Delta y \delta_{yy})][\mathbf{I} + \Delta t(\delta_z C - \delta_{zz} Y - \varepsilon_i \Delta z \delta_{zz})]\Delta Q \\ = -\Delta t[A\delta_x - R\delta_{xx} - R_1\delta_{yx} - R_2\delta_{zx} \\ + B\delta_y - S_1\delta_{xy} - S\delta_{yy} - S_2\delta_{zy} \\ + C\delta_z - Y_1\delta_{xz} - Y_2\delta_{yz} - Y\delta_{zz} \\ + \varepsilon_e(\Delta x^3 \delta_{xxxx} + \Delta y^3 \delta_{yyyy} + \Delta z^3 \delta_{zzzz})]Q.\end{aligned} \tag{35}$$

The corresponding factorization for the Euler equations becomes apparent if the viscous flux Jacobians R, R_1, R_2, S, S_1, S_2, Y, Y_1, Y_2 are set to zero.

Other approximate factorizations that are considered in this work are those formulated for the Euler equations in [18] and [19], viz.,

$$\begin{aligned}[\mathbf{I} + \Delta t(\delta_x^- A^+ + \delta_x^+ A^-)][\mathbf{I} + \Delta t(\delta_y^- B^+ + \delta_y^+ B^-)] \\ [\mathbf{I} + \Delta t(\delta_z^- C^+ + \delta_z^+ C^-)]\Delta Q = -\Delta t R^n\end{aligned} \tag{36}$$

$$\begin{aligned}[\mathbf{I} + \Delta t(\delta_x^- A^+ + \delta_y^- B^+ + \delta_z^- C^+)][\mathbf{I} + \Delta t(\delta_x^+ A^- \\ + \delta_y^+ B^- + \delta_z^+ C^-)]\Delta Q = -\Delta t R^n\end{aligned} \tag{37}$$

$$\begin{aligned}[\mathbf{I} + \Delta t(\delta_x^- A^+ + \delta_x^+ A^- + \delta_z^- C^+)][\mathbf{I} + \Delta t(\delta_y^- B^+ \\ + \delta_y^+ B^- + \delta_z^+ C^-)]\Delta Q = -\Delta t R^n,\end{aligned} \tag{38}$$

where

$$\begin{aligned}R^n = \delta_x^- E^+ + \delta_x^+ E^- + \delta_y^- F^+ \\ + \delta_y^+ F^- + \delta_z^- G^+ + \delta_z^+ G^-\end{aligned} \tag{39}$$

$$\begin{aligned}[\mathbf{I} + \Delta t(\delta_x^- A_1 + \delta_y^- B_1 + \delta_z^- C_1) + \kappa_2 \Delta t(\delta_x^- + \delta_y^- + \delta_z^-)] \\ \times [\mathbf{I} + \Delta t(\delta_x^+ A_2 + \delta_y^+ B_2 + \delta_z^+ C_2) \\ - \kappa_2 \Delta t(\delta_x^+ + \delta_y^+ + \delta_z^+)] \\ = -\Delta t(\delta_x E + \delta_y F + \delta_z G) - \kappa_4 \Delta t(\Delta x^3 \delta_{xxxx} \\ + \Delta y^3 \delta_{yyyy} + \Delta z^3 \delta_{zzzz}).\end{aligned} \tag{40}$$

Equations (36), (37), and (38) are upwind schemes, and are referred to as spatial, eigenvalue, and combination factorizations, respectively. The flux-vector splitting methods of Steger and Warming [23] and van Leer [24] are assumed. Equation (40) is the Lower and Upper (LU) factorization. Here, the fluxes devised by Jameson and Turkel [25], viz., $A_1 = (A + |A|)/2$ and $A_2 = (A - |A|)/2$,

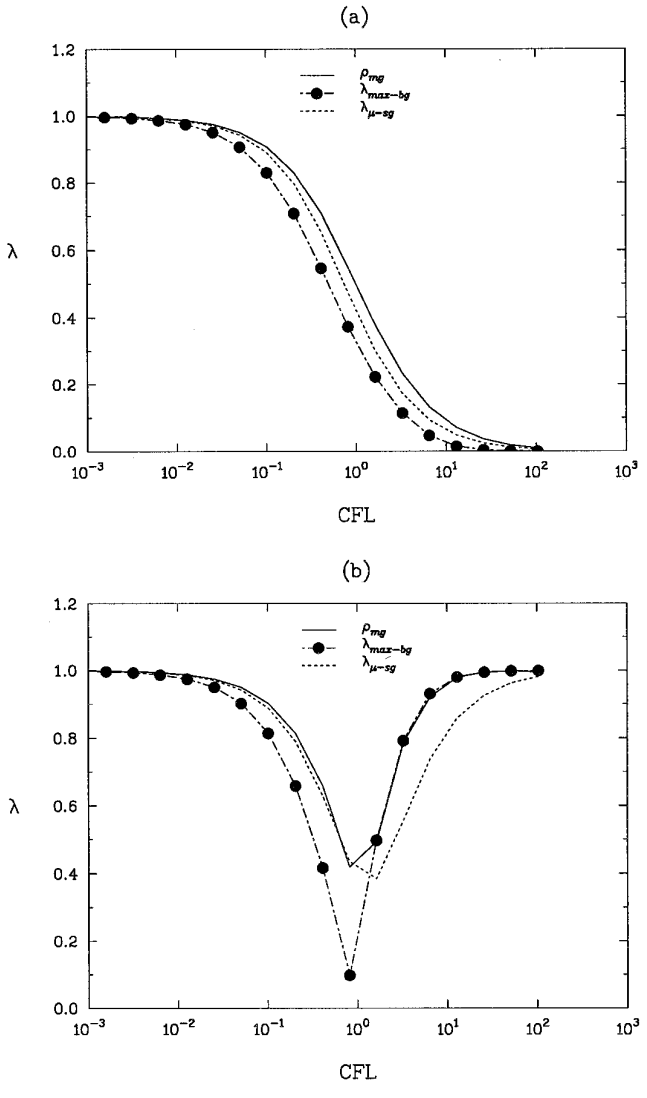

FIG. 5. Convergence characteristics for 1-D convection equation: (a) implicit; (b) semi-implicit time integrations (Dirichlet B.C.'s).

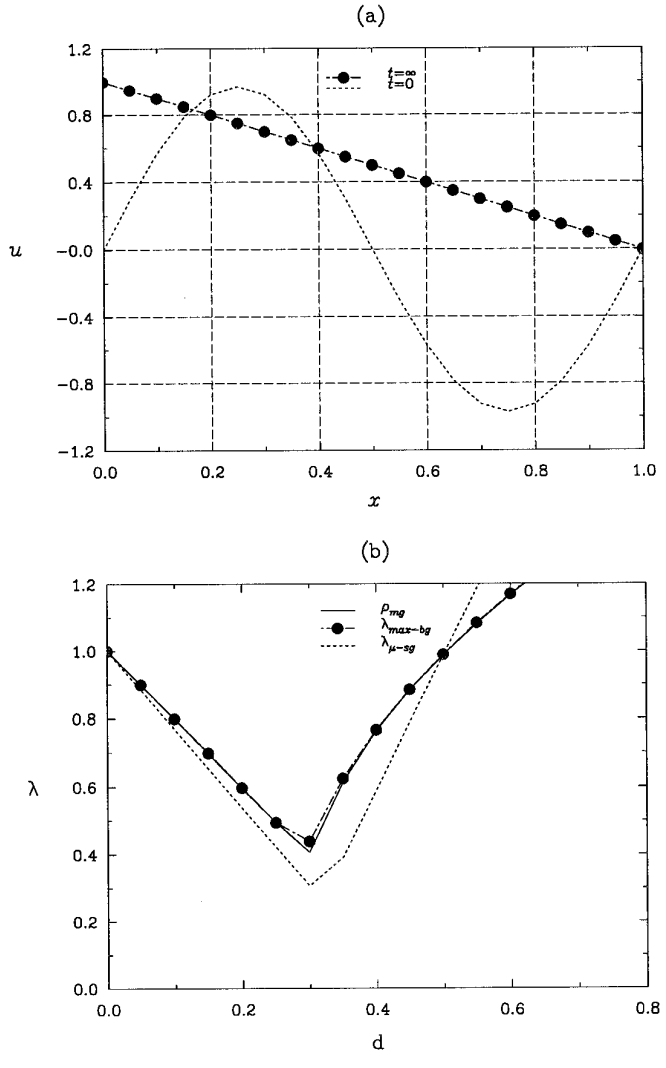

FIG. 6. 1-D diffusion equation: (a) steady solution; (b) convergence characteristics (Euler forward explicit; Dirichlet B.C.'s).

are used to achieve diagonal dominance. δ^+ and δ^- denote forward and backward difference operators, respectively, and κ_2 and κ_4 are the artificial dissipation coefficients.

Fourier Symbols

The bi-grid amplification matrix $\hat{M}(\Theta)$ is constructed from $M = S_2^{v^2}(I - I_H^h L_H^{-1} I_h^H L_h) S_1^{v^1}$. For ease of presentation, the Euler equations alone are selected for illustration, with the ADI central scheme used as the smoother. In this case, the viscous fluxes R, R_1, R_2, S, S_1, S_2, Y, Y_1, Y_2 are set to zero. The components operators of matrix $\hat{M}(\Theta)$ are:

(i) *The Fine/Coarse Grid Operator* $\hat{L}$. The Euler equivalent form of Eq. (31) is

$$\frac{\partial Q}{\partial t} = -\left(\frac{\partial E}{\partial x} + \frac{\partial F}{\partial y} + \frac{\partial G}{\partial z}\right) + \text{dissipation}. \tag{41}$$

Thus, in quasi-linear form,

$$\begin{aligned} L(Q) = &-\left(A\frac{\partial Q}{\partial x} + B\frac{\partial Q}{\partial y} + C\frac{\partial Q}{\partial z}\right) \\ &+ \varepsilon_i\left(\Delta x\frac{\partial^2 Q}{\partial x^2} + \Delta y\frac{\partial^2 Q}{\partial y^2} + \Delta z\frac{\partial^2 Q}{\partial z^2}\right) \\ &-\varepsilon_e\left(\Delta x^3\frac{\partial^4 Q}{\partial x^4} + \varepsilon y^3\frac{\partial^4 Q}{\partial y^4} + \Delta z^3\frac{\partial^4 Q}{\partial z^4}\right). \end{aligned} \tag{42}$$

Holding A, B, C locally constant and employing second-

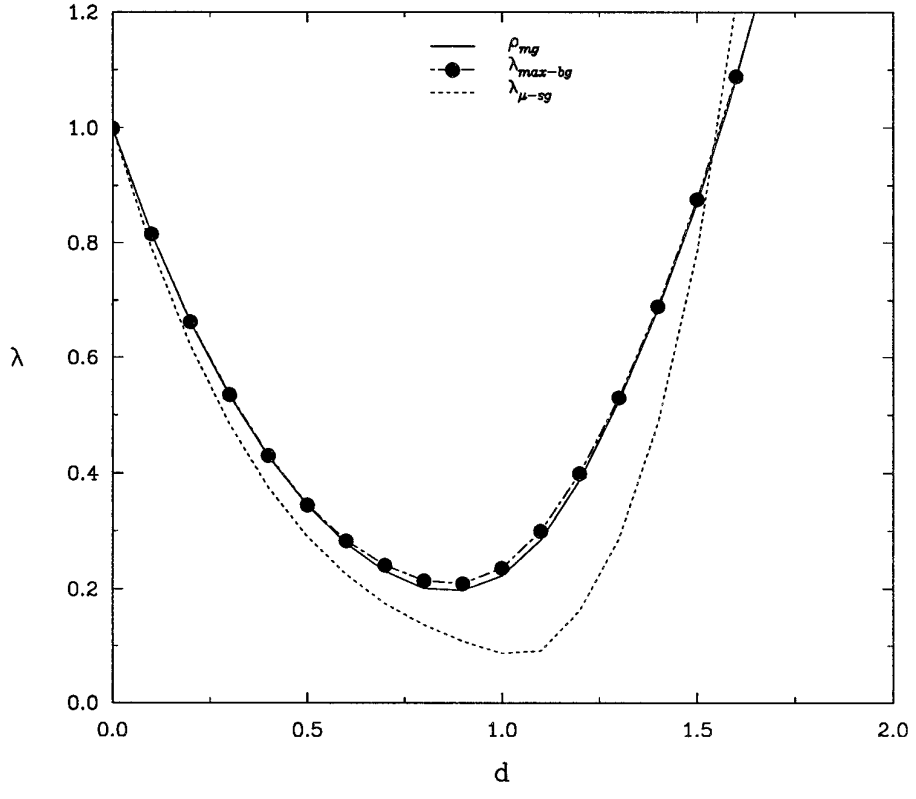

FIG. 7. Convergence characteristics for 1-D diffusion equation (4-stage Runge–Kutta; Dirichlet B.C.'s; van Leer coefficients).

order central differencing, the Fourier symbol of the fine grid problem on equal mesh size in all directions becomes

$$\hat{L}_h(\Theta^m) = -\frac{I}{\Delta x}[A\sin(\Theta_1^m) + B\sin(\Theta_2^m) + C\sin(\Theta_3^m)] + \frac{2\varepsilon_i}{\Delta x}[\cos(\Theta_1^m) + \cos(\Theta_2^m) + \cos(\Theta_3^m) - 3] - \frac{16\varepsilon_e}{\Delta x}\left[\sin^4\left(\frac{\Theta_1^m}{2}\right) + \sin^4\left(\frac{\Theta_2^m}{2}\right) + \sin^4\left(\frac{\Theta_3^m}{2}\right)\right] \quad (m = 1, 8). \quad (43)$$

Note that Θ_k^m represent the k^{th} element of the Θ^m component (see Eqs. (9)–(11)).

For any arbitrary mode, Eq. (43) is a 40×40 matrix since each Jacobian is a 5×5 matrix and there are eight harmonics including the fundamental mode. The coarse grid problem is assumed to be a version of the original problem on the fine grid and the coarse grid is formed simply by deleting every other fine grid point. Thus, the mesh size and Fourier modes are $\{2\Delta x, 2\Theta^1\}$ and its Fourier signature can be written as

$$\hat{L}_H(2\Theta^1) = -\frac{I}{2\Delta x}[A\sin(2\theta_x) + B\sin(2\theta_y) + C\sin(2\theta_z)] + \frac{\varepsilon_i}{\Delta x}[\cos(2\theta_x) + \cos(2\theta_y) + \cos(2\theta_z) - 3] - \frac{8\varepsilon_e}{\Delta x}(\sin^4\theta_x + \sin^4\theta_y + \sin^4\theta_z). \quad (44)$$

In the above equation, only the fundamental mode, $\Theta^1 = \{\theta_x, \theta_y, \theta_z\}$, is employed since the coarse grid problem is assumed to be solved exactly. Hence, this is only a 5×5 matrix.

(ii) *The Relaxation Operator* $\hat{S}$. Each of Eqs. (35), (36), (37), (38), and (40) can be expressed as

$$N\Delta Q^n = -L = -\Delta t R^n \quad (45)$$

Von Neumann stability analysis is used on this system of linear equations by letting the step-by-step solution be characterized by

$$Q^n = U_o \lambda^n e^{Ii\theta_x} e^{Ij\theta_y} e^{Ik\theta_z}, \quad (46)$$

where λ is the single grid amplification factor. Thus, Eq.

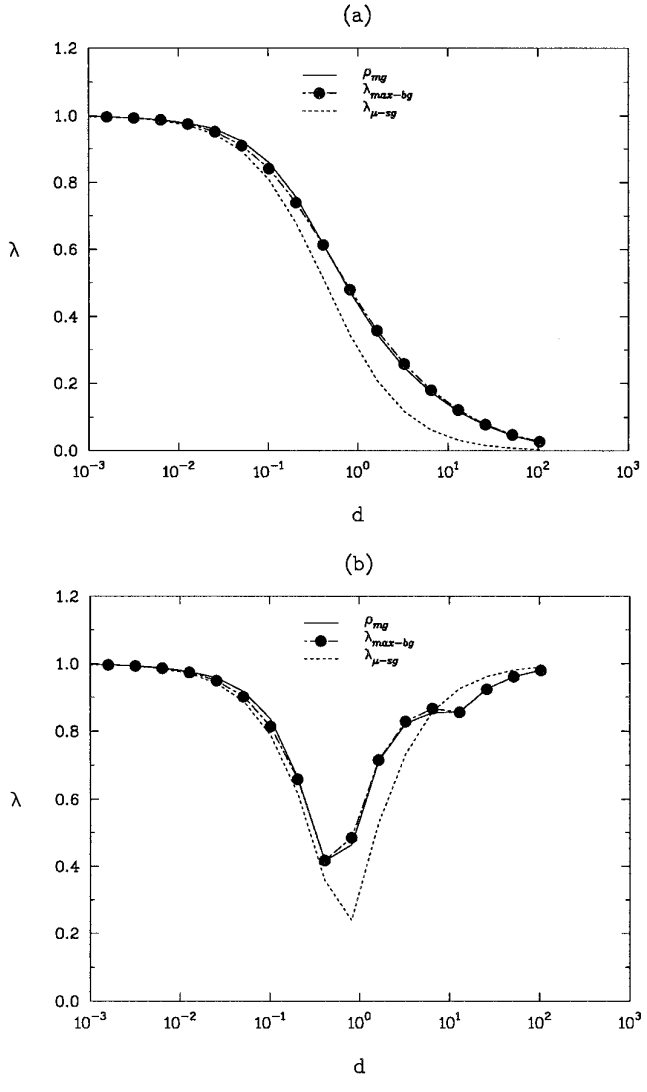

FIG. 8. Convergence characteristics for 1-D diffusion equation: (a) implicit; (b) semi-implicit time integrations (Dirichlet B.C.'s).

(45) reduces to a complex generalized eigenvalue problem of the form

$$\hat{K}\mathbf{x} = \lambda\hat{N}\mathbf{x} \quad \textit{where } \hat{K} = \hat{N} - \hat{L}. \tag{47}$$

The Fourier symbols of $\hat{N}$ and $\hat{L}$, for our particular example, can easily be shown to be

$$\hat{N}(\Theta^m) = \left[\mathbf{I} + \frac{\Delta t}{\Delta x}\left(AI\sin(\Theta_1^m) + 4\varepsilon_i \sin^2\frac{\Theta_1^m}{2}\right)\right] \left[\mathbf{I} + \frac{\Delta t}{\Delta y}\left(BI\sin(\Theta_2^m) + 4\varepsilon_i \sin^2\frac{\Theta_2^m}{2}\right)\right] \left[\mathbf{I} + \frac{\Delta t}{\Delta z}\left(CI\sin(\Theta_3^m) + 4\varepsilon_i \sin^2\frac{\Theta_3^m}{2}\right)\right] \tag{48}$$

$$\hat{L}(\Theta^m) = \frac{\Delta t}{\Delta x} I(A\sin(\Theta_1^m) + B\sin(\Theta_2^m) + C\sin(\Theta_3^m)) + \frac{16\Delta t\varepsilon_e}{\Delta x}\left(\sin^4\frac{\Theta_1^m}{2} + \sin^4\frac{\Theta_2^m}{2} + \sin^4\frac{\Theta_3^m}{2}\right). \tag{49}$$

The Fourier symbols corresponding to the other approximate factorizations are documented in Demuren and Ibraheem [26]. For each harmonic, Θ^m ($m = 1, 8$), Eq. (47) is solved to give five eigenvalues from which the elements of $\hat{S}(\Theta)$ are constructed. For example, if the eigenvalues corresponding to the mode $\Theta^1 = \{\theta_x, \theta_y, \theta_z\}$ are $\Lambda = \{\lambda_1, \lambda_2, \lambda_3, \lambda_4, \lambda_5\}$, then, from Eq. (11), $\hat{S}(\Theta^1) = \Lambda\mathbf{I}$. The effective fine grid smoothing operation is obtained by raising the smoothing matrices to the power of v^1 and v^2, the pre- and post-smoothing counts, respectively.

(iii) *The Transfer Operators $\hat{I}_H^h$ and $\hat{I}_h^H$.* For a second-order interpolation, the Fourier symbol of the prolongation operator, from Eq. (12), is

$$\hat{I}_H^h(\Theta^m) = \tfrac{1}{8}[1 + \cos(\Theta_1^m)][1 + \cos(\Theta_2^m)][1 + \cos(\Theta_3^m)]. \tag{50}$$

The restriction operator, $\hat{I}_h^H$, is computed from Eqs. (50) and (13), assuming full weighting.

Based on the above operators, $\hat{M}(\Theta)$ is assembled from $M = S_2^{v^2}(I - I_H^h L_H^{-1} I_h^H L_h) S_1^{v^1}$. A symbolic form is given in Appendix A. It is an 8×8 block matrix of which each elemental block is a 5×5 matrix.

Solution Procedure

The eigenvalues for the bi-grid matrix $\hat{M}(\Theta)$ are computed from Eq. (8) over fixed Fourier modes to obtain the amplification factor. Sixteen modes are selected, in the range $-\pi/2 \le \Theta^1 \le \pi/2$. The smoothing factor is also computed from the generalized eigenvalue problem (47) over only the high-frequency modes $\pi/4 \le |\Theta^1| < \pi/2$ as $\lambda_{\mu\_sg} = \max(|\lambda|)$. In each case, the eigenvalues are solved for using the linear algebra routines such as found in the IMSL library. Uniform flow is assumed with $M_\infty = 0.8$, zero yaw (α_y) and angle of attack (α_a), and $\gamma = 1.4$. Further, the grid spacing is assumed to be uniform in all directions. Effects of aspect ratio and flow skewness are also investigated. The time-step and Reynolds number are calculated from

$$\Delta t = \mathrm{CFL}\Big/\left[\frac{|u|}{\Delta x} + \frac{|v|}{\Delta y} + \frac{|w|}{\Delta z} + c\sqrt{\frac{1}{\Delta x^2} + \frac{1}{\Delta y^2} + \frac{1}{\Delta z^2}}\right] \tag{51}$$

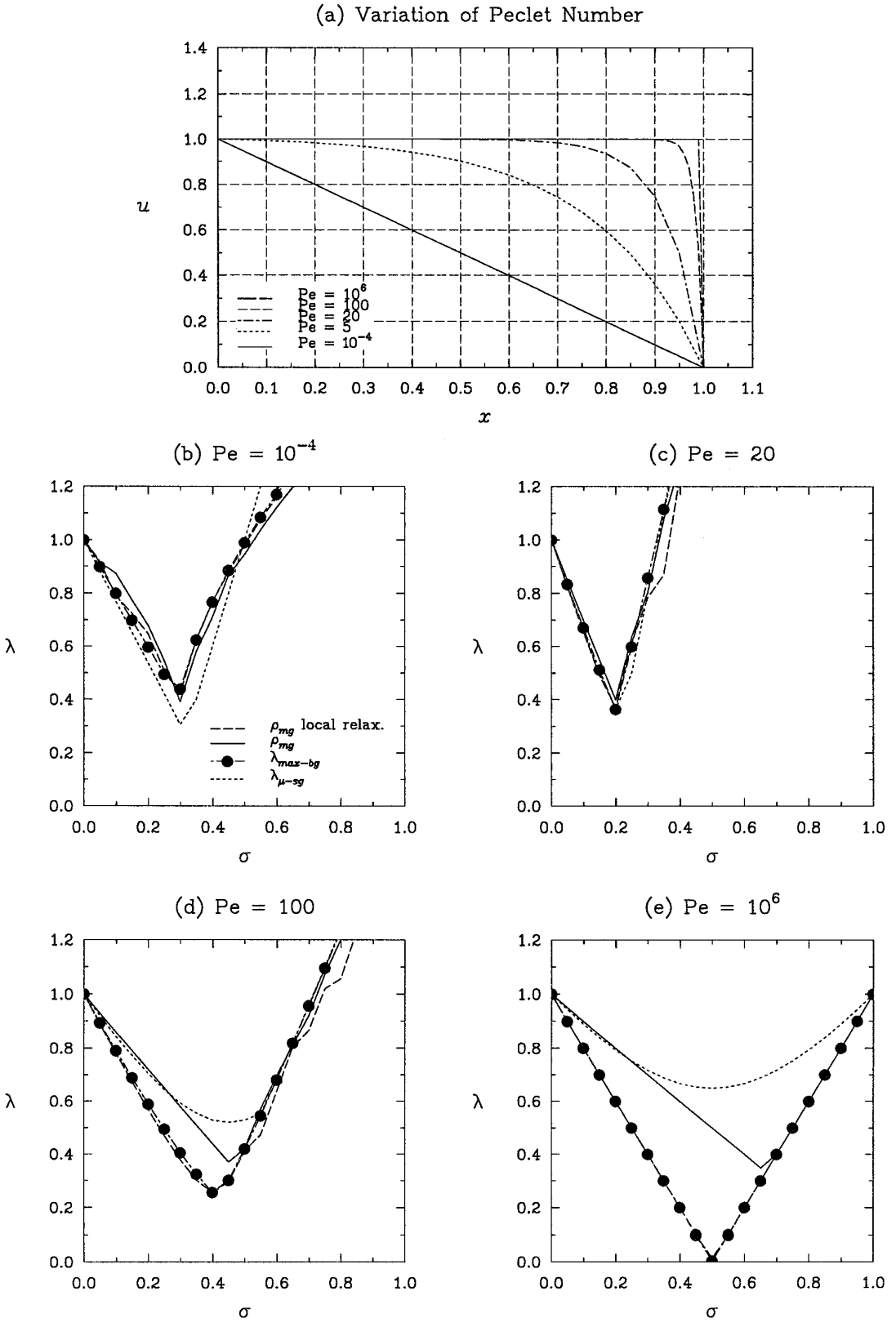

FIG. 9. 1-D linear Burger's equation: (a) steady solution; (b)–(e) convergence characteristics (Euler forward explicit; first order accurate).

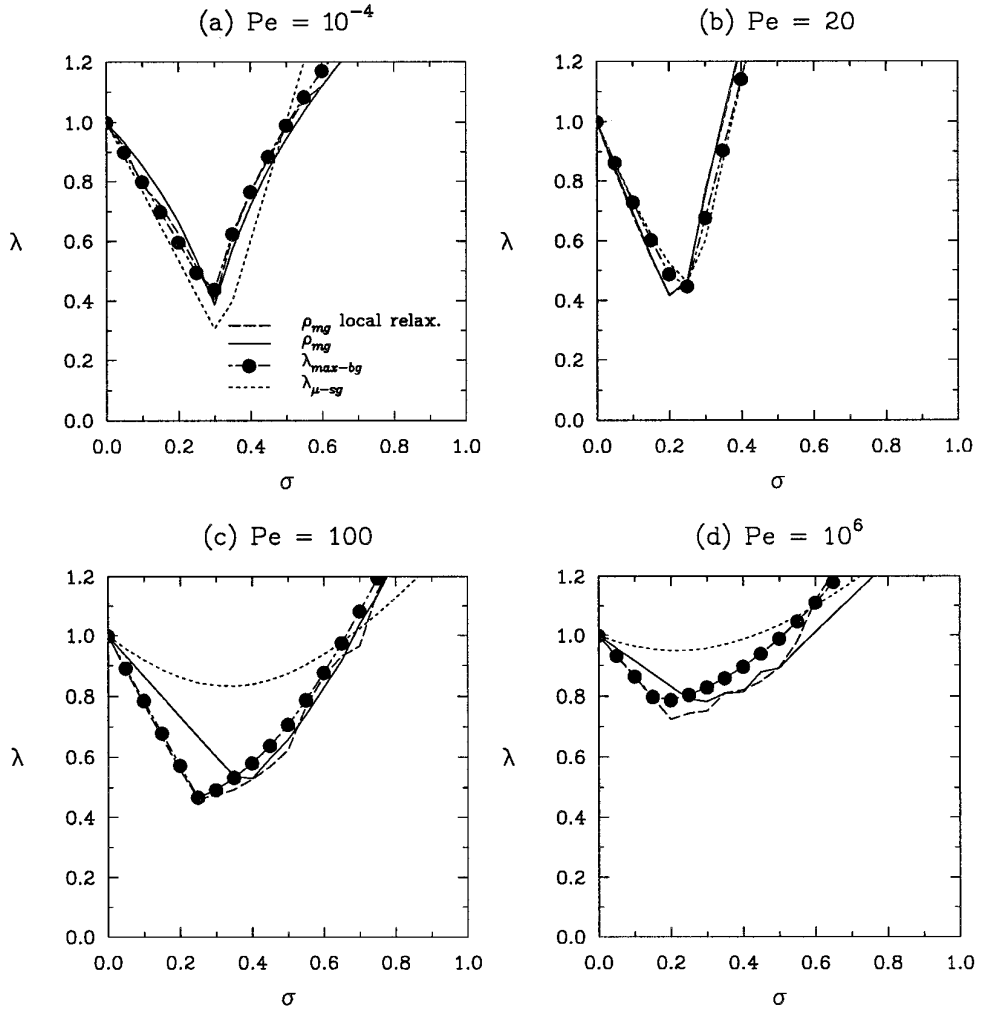

FIG. 10. 1-D linear Burger's equation: (a)–(d) convergence characteristics (Euler forward explicit; second order accurate).

$$\mathrm{Re} = \frac{\rho |V| (\sqrt{\Delta x^2 + \Delta y^2 + \Delta z^2})}{\mu}. \tag{52}$$

Some other pertinent definitions used are as follows:

$$|V| = \sqrt{u^2 + v^2 + w^2}, \quad M_\infty = \frac{|V|}{a},$$
$$v = u \tan(\alpha_y), \quad w = u \tan(\alpha_a). \tag{53}$$

Practical Convergence Rates

Practical multigrid solutions are obtained for inviscid and viscous flows around a circular cylinder using the PROTEUS computer code developed at NASA Lewis Research Center by Towne *et al.* [27]. We implemented the FAS-FMG (full approximate storage-full Multigrid) algorithm applicable to non-linear systems of equations in the PROTEUS code. This code is based on the ADI Beam–Warming scheme. The asymptotic convergence rate of these flows were computed from Eq. (28). The Reynolds number based on the cylinder diameter is 20 and the Mach number is 0.2. The grid size for the inviscid flow is 25 × 49 and 49 × 49 for the viscous flow. In each case, the grid was clustered such that the aspect ratio varied from 1.5 to 3.8 for the inviscid flow and 0.5 to 12.2 for the viscous flow. Further, pre- and post-smoothing counts are 1 and 0, respectively; the same as assumed in the analyses. In order to ascertain the suitability of bi-grid and smoothing factors in predicting multigrid performance in complex flows, asymptotic convergence rates are computed from practical multigrid solutions of the 2-D Euler and Navier–Stokes equations, respectively, in these flows. The steady-state solutions are shown in Fig. 13a. Rather than evaluating the corresponding bi-grid and smoothing factors from uniform flow conditions, as described above, they are computed at each point in the flow field using frozen coeffi-

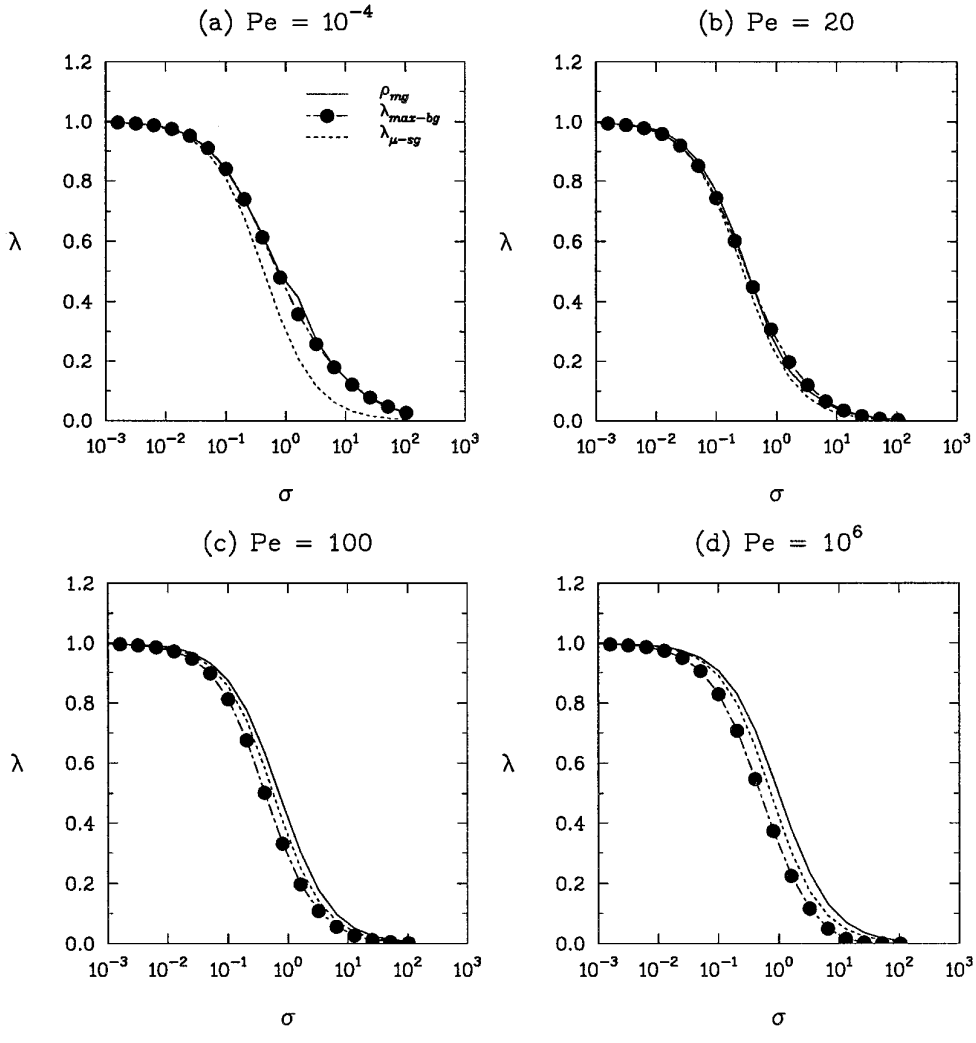

FIG. 11. 1-D linear Burger's equation: (a)–(d) convergence characteristics (implicit time integration).

cients, thereby accounting for the variation in flow properties. Figures 13b and 13c show estimates from both the analyses and practical multigrid convergence rates for the inviscid and viscous flows, respectively. These results are also summarized in Table I. For both flow problems, the smoothing factor gives a much poorer prediction of the practical solution than does the bi-grid factor.

Convergence results for the various upwind difference schemes given by Eqs. (36)–(38) are considered next. For these and subsequent results, uniform flow conditions as described under Solution Procedure above are utilized in the single grid and the bi-grid analyses. Results for the Steger–Warming flux–vector splitting are presented in Figs. 14a–14c, and those for the van Leer flux–vector splitting in Figs. 14d–14f. For the latter, practical multigrid convergence rates were obtained by Anderson *et al.* [18], for transonic flow over an ONERA M8 wing at a free-stream Mach number of 0.84, angle of attack of 3.06°, and a mesh size 97 × 17 × 17. Optimal CFL numbers and convergence rates are tabulated in Table II. For each scheme, the bi-grid analysis predicted the correct optimum CFL number of 7, whereas the smoothing factor obtained from single grid analysis predicted the incorrect optimum value of 3. The convergence rates were also correctly predicted by the bi-grid analysis, whereas the smoothing factors gave values that were much too optimistic. Anderson *et al.* [18] had only utilized the smoothing factor in their analysis, and thus could not properly predict the conditions for optimum multigrid performance. The present work is clearly an improvement, which will aid the development of practical multigrid methods. A comparison of predicted convergence rates in Fig. 14 shows that the van Leer splitting generally lead to more stable schemes and faster convergence rates than the Steger–Warming splitting.

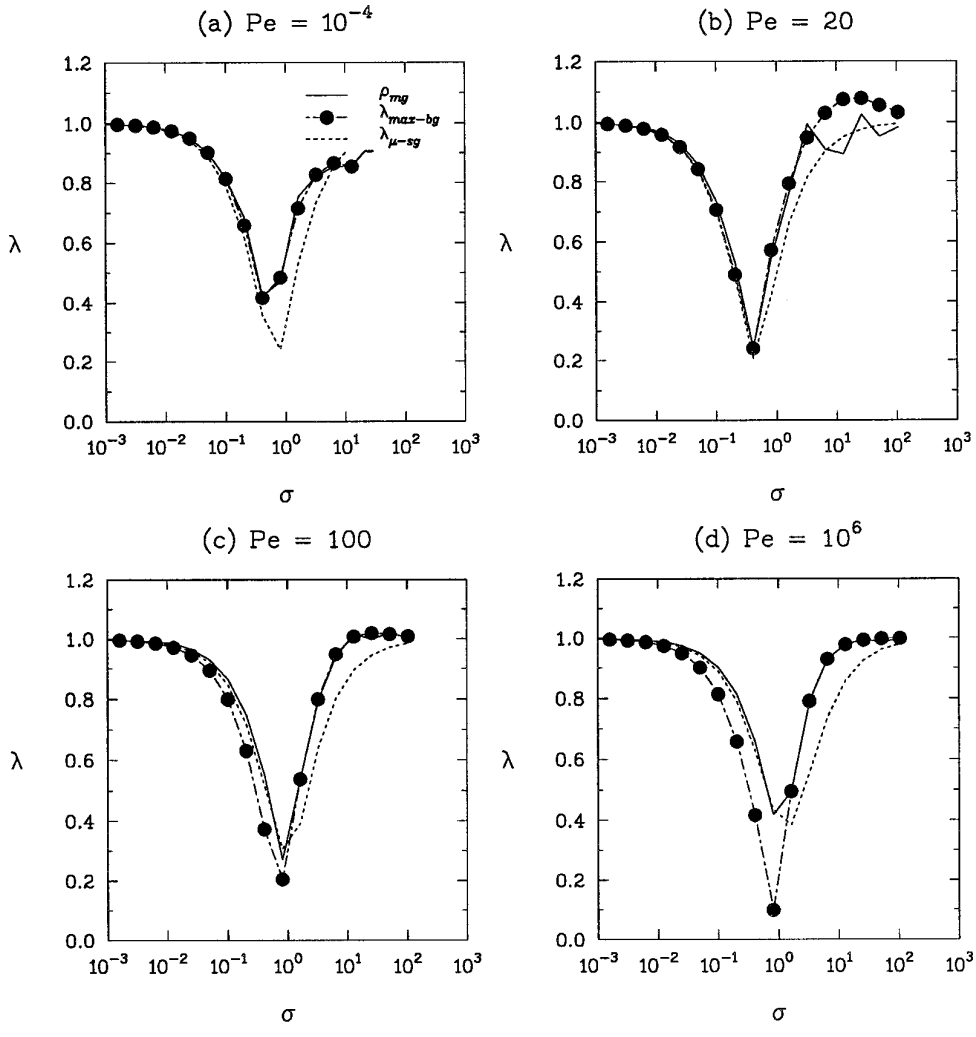

FIG. 12. 1-D linear Burger's equation: (a)–(d) convergence characteristics (semi-implicit time integration).

Further Results

Results for the 3-D Euler equations using the LU approximate factorization with central difference approximation and various levels of second- and fourth-order artificial viscosities, κ_2 and κ_4, are shown in Figs. 15a–15c. Without the addition of second-order dissipations, i.e., $\kappa_2 = 0$, the coefficients $\kappa_4 = 0.3$ yields the optimal results (see Fig. 15a). From Figs. 15b and 15c, bi-grid and smoothing factors predict that an appropriate combination of κ_2 and κ_4 (especially when $\kappa_4 \geq \kappa_2$) can significantly improve the performance of the (LU) scheme when used as a relaxation scheme for multigrid. Also for all levels of dissipation, the smoothing factors estimates are more optimistic than the bi-grid results, especially at lower CFL numbers.

The convergence characteristics for the 3-D Euler and Navier–Stokes equations for different levels of artificial dissipation and Reynolds numbers are shown in Figs. 15d–15f and 16, using the Beam–Warming (ADI) central difference scheme as the baseline solution algorithm. With no dissipation added to the Euler equations (Fig. 15d), the bi-grid analysis predicts instability for all CFL numbers, while the smoothing factor predicts stability for CFL numbers below 15. From Figs. 15e and 15f, optimal multigrid performance is predicted by the bi-grid analysis for dissipation levels of $\varepsilon_e = 0.5$ and $\varepsilon_i = 1.0$. These results are similar to those obtained for the Navier–Stokes equations at Re = 10^6 (see Figs. 16d–16f). With a Reynolds number of 100 and no dissipation, both bi-grid and smoothing factors predict stability for certain range of CFL numbers, although the latter is more optimistic. Also at this Reynolds number, the optimal dissipation levels are $\varepsilon_e = 0.5$ and $\varepsilon_i = 1.0$.

All computations have been based on zero yaw and angle of attack, and also on uniform grid spacing in all directions. Sensitivities of convergence characteristics to flow skewness and aspect ratio are studied using the ADI

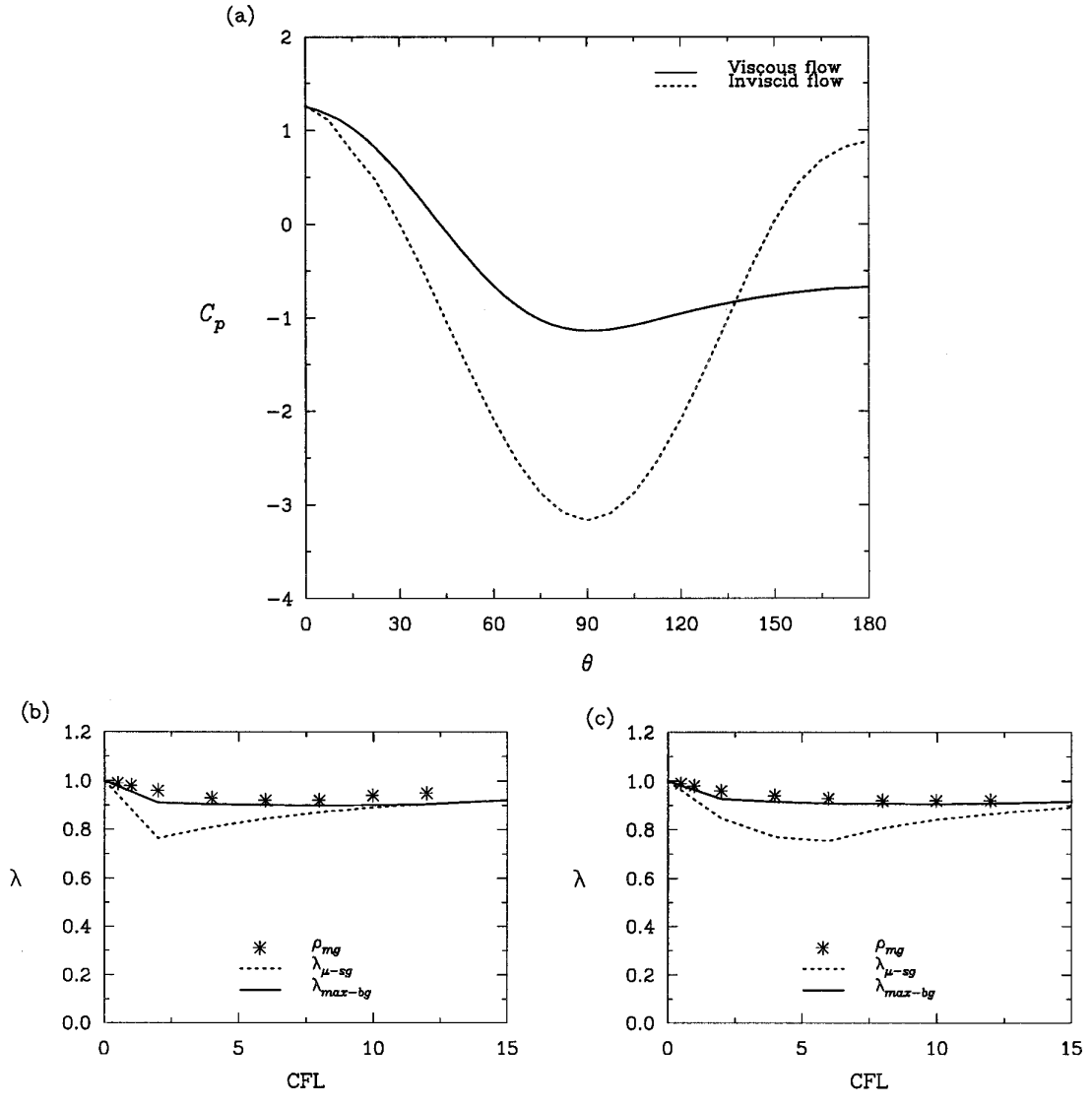

FIG. 13. 2-D Euler and Navier–Stokes flows around a circular cylinder using ADI central schemes ($\varepsilon_e = 1$, $\varepsilon_i = 2$, $\nu^1 = 1$, $\nu^2 = 0$).

TABLE I

Convergence Characteristics of 2-D Euler and Viscous Flows around a Cylinder

	Euler			Viscous flow		
CFL	λ_{μ_sg}	$\lambda_{\max\_bg}$	ρ_{mg}	λ_{μ_sg}	$\lambda_{\max\_bg}$	ρ_{mg}
0.5	0.88	0.94	0.99	0.95	0.96	0.99
1.0	0.80	0.92	0.98	0.91	0.94	0.98
2.0	0.76	0.91	0.96	0.85	0.93	0.96
4.0	0.81	0.90	0.93	0.77	0.92	0.94
6.0	0.84	0.90	0.92	0.76	0.91	0.93
8.0	0.87	0.90	0.92	0.81	0.91	0.92
10.0	0.89	0.90	0.94	0.84	0.91	0.92
12.0	0.91	0.90	0.95	0.87	0.91	0.92

TABLE II

Optimum CFL and Convergence Rates for Transonic Flow over ONERA M8 Wing

	Spatial	Eigenvalue	Combination	Comment
$(\text{CFL}, \lambda)_{\mu-sg}$	3, 0.76	3, 0.80	4, 0.75	single grid analysis
$(\text{CFL}, \lambda)_{\max-\sigma g}$	7, 0.89	7, 0.91	7, 0.89	bi-grid analysis
$(\text{CFL}, \rho)_{mg}$	7, 0.90	7, 0.93	7,	From Andersen *et al.* [18]

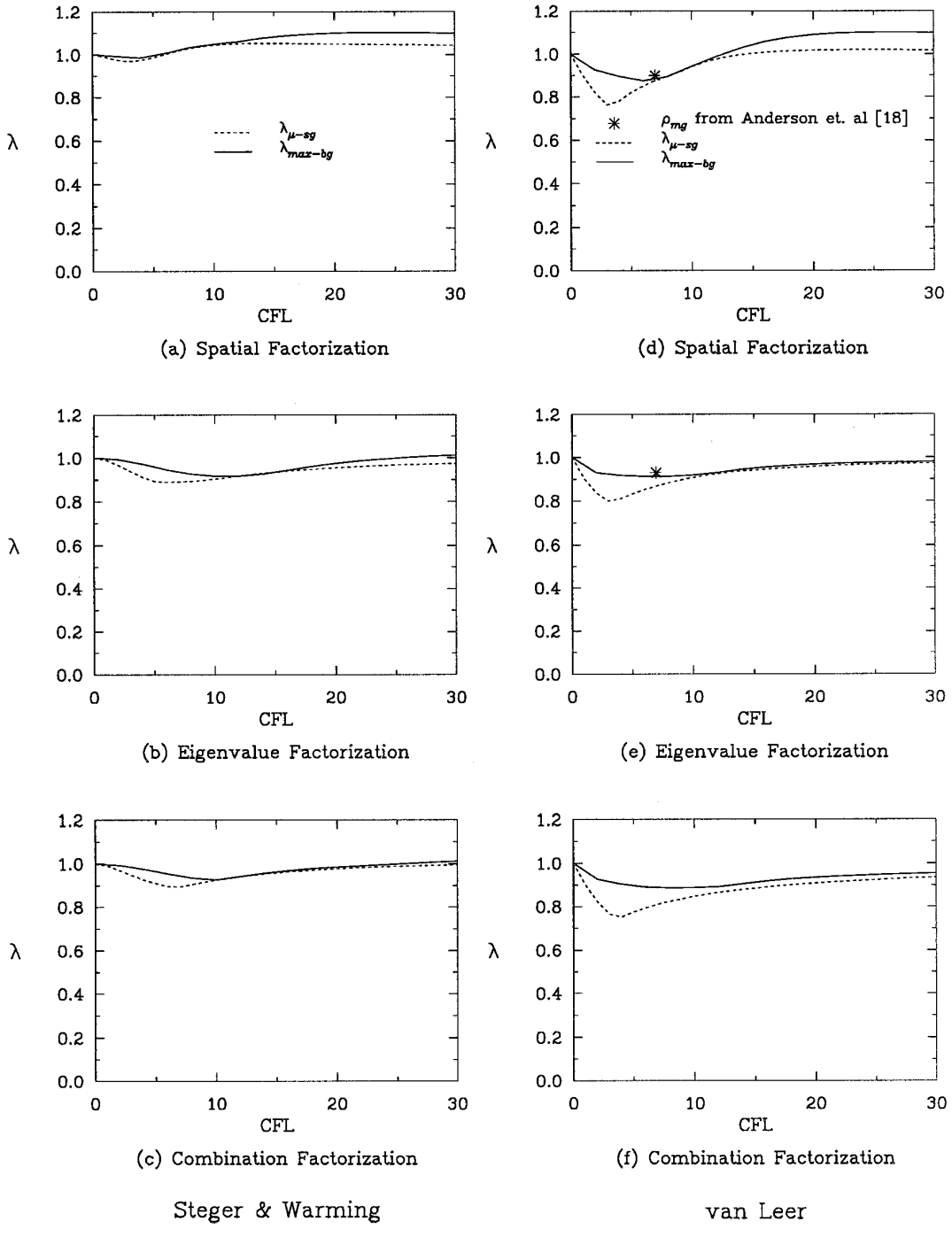

FIG. 14. 3-D Euler equations using upwind schemes: (a)–(f) convergence characteristics ($\nu^1 = 1$; $\nu^2 = 0$).

central scheme at Reynolds number of 100, and dissipation levels of $\varepsilon_e = 0.5$ and $\varepsilon_i = 1.0$. The results are shown in Figs. 17 and 18. Generally, convergence characteristics are improved with increases in yaw angle at zero angle of attack although the range of stable CFL numbers becomes smaller (Figs. 17a–17c). From Figs. 17d–17f, no significant difference is observed in the convergence results when the yaw and angle of attack are set equal to each other. From Fig. 18, the convergence characteristics become worse with increases in grid aspect ratio.

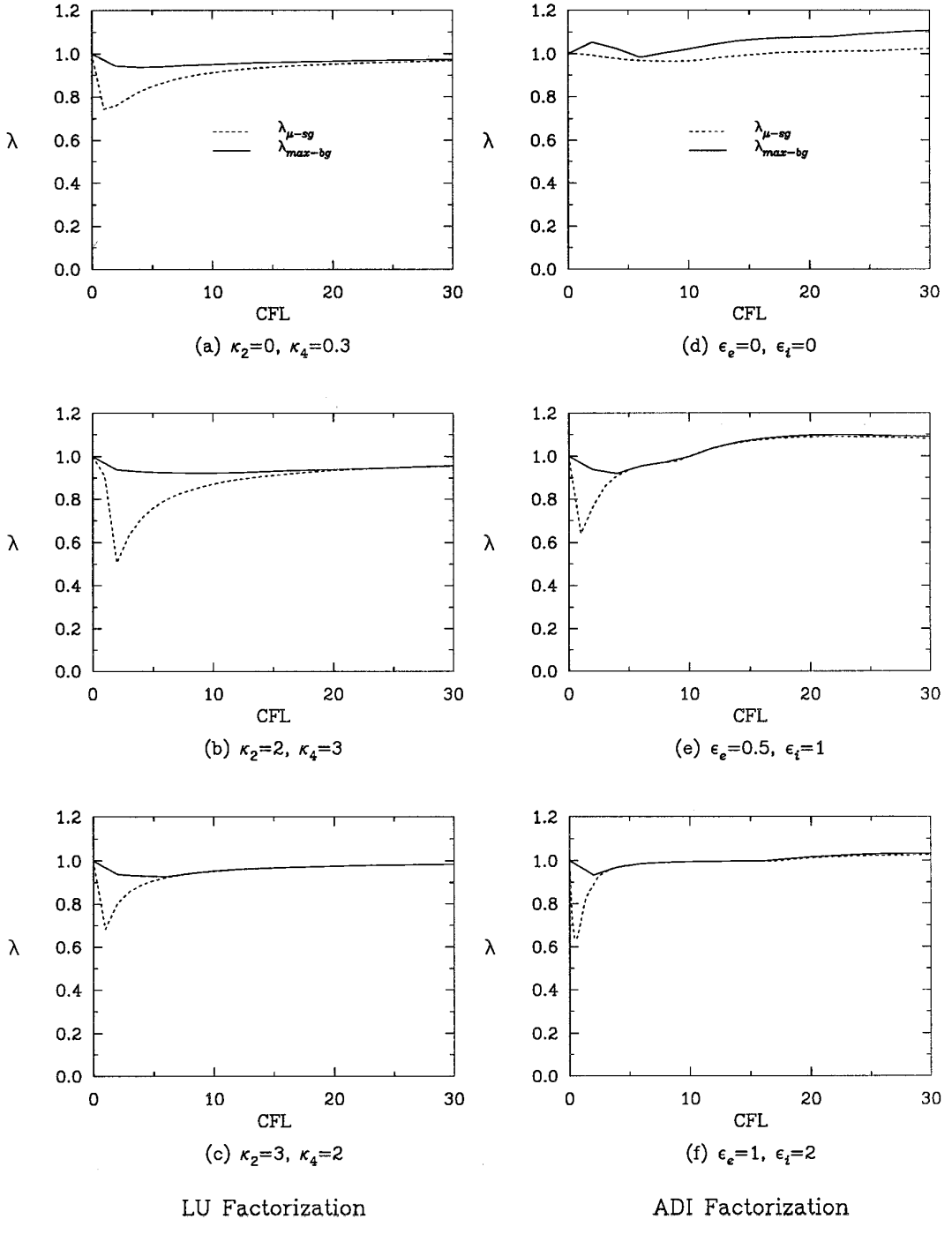

FIG. 15. 3–D Euler equations using central schemes: (a)–(f) convergence characteristics ($\nu^1 = 1$; $\nu^2 = 0$).

5. CONCLUDING REMARKS

Bi-grid stability analysis has been presented for typical explicit and implicit solution methods for 1-D model problems which range from the diffusion equation to the convection equation and including the convection–diffusion equation at different Peclet numbers. Bi-grid amplification factors were compared with smoothing factors and multigrid convergence rates. The predicted bi-grid amplification factors agree quite well with the asymptotic convergence rate of the multigrid method. The smoothing rate of the relaxation scheme obtained from

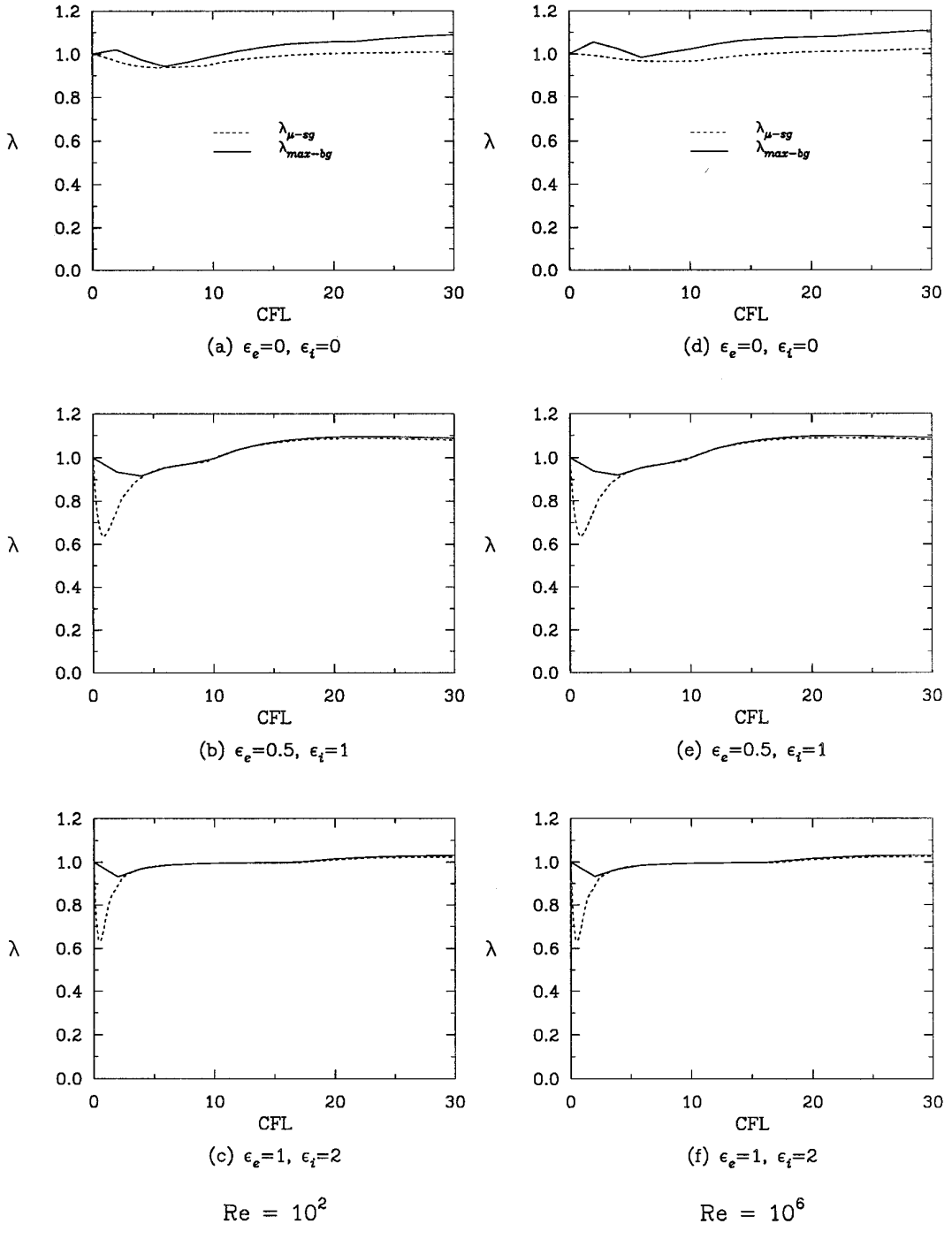

FIG. 16. 3–D Navier–Stokes equations using central schemes: (a)–(f) convergence characteristics ($\nu^1 = 1$; $\nu^2 = 0$).

a local mode analysis on a single grid is not an accurate predictor of the multigrid convergence rate. For multigrid performance in large scale practical computations, bi-grid amplification factor and smoothing factor were computed for multidimensional Euler and Navier–Stokes equations. Various approximate factorization methods that are popular in practice are considered. In typical practical multigrid solutions of 2-D inviscid and viscous flow and 3-D transonic flow problems, bi-grid analysis was shown to give better prediction of the convergence rate than the smoothing factor obtained from a single grid analysis.

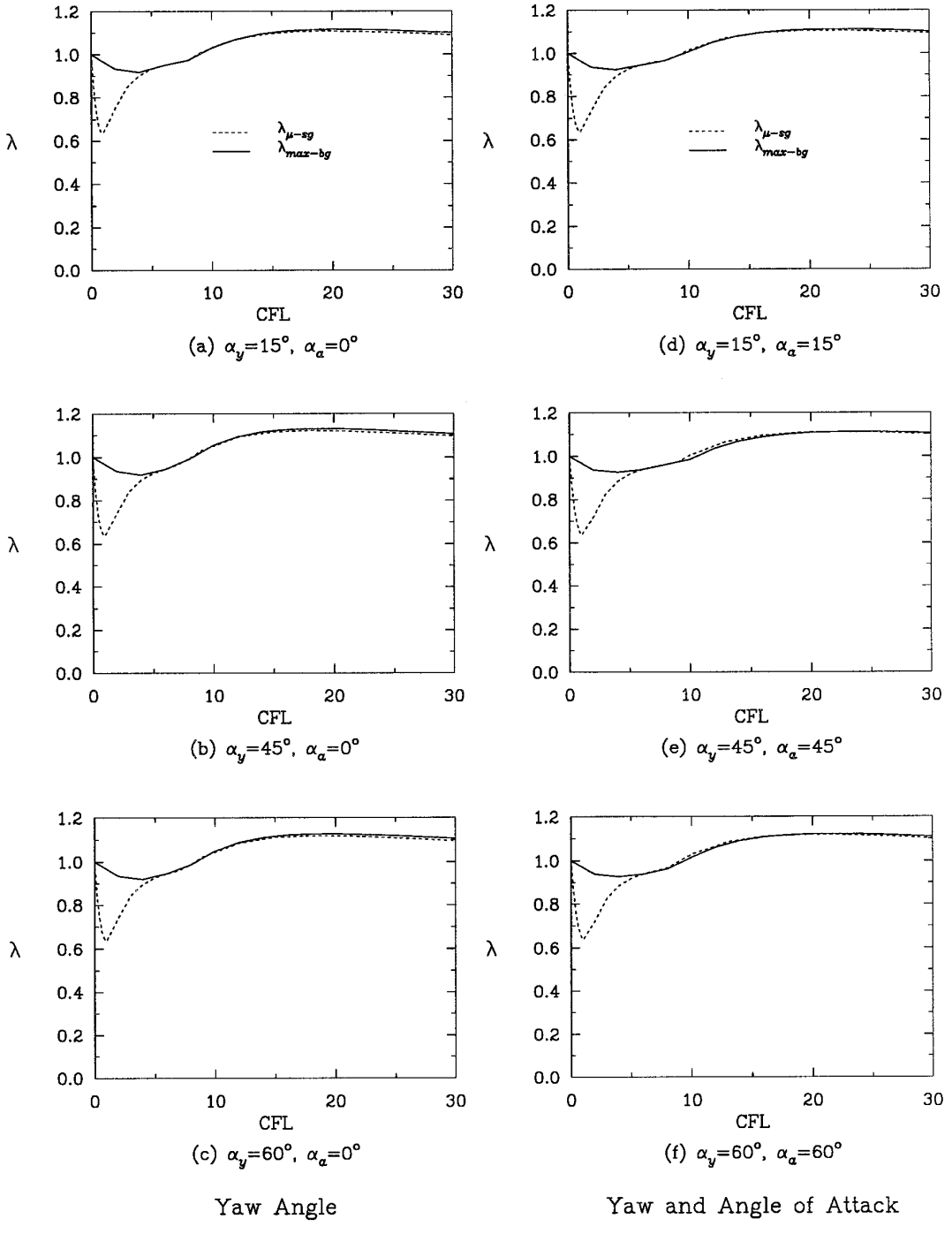

FIG. 17. 3-D Navier–Stokes equations using central schemes: (a)–(f) convergence characteristics—flow skewness (Re = 100, ε_e = 0.5, ε_i = 1.0, ν^1 = 1, ν^2 = 0).

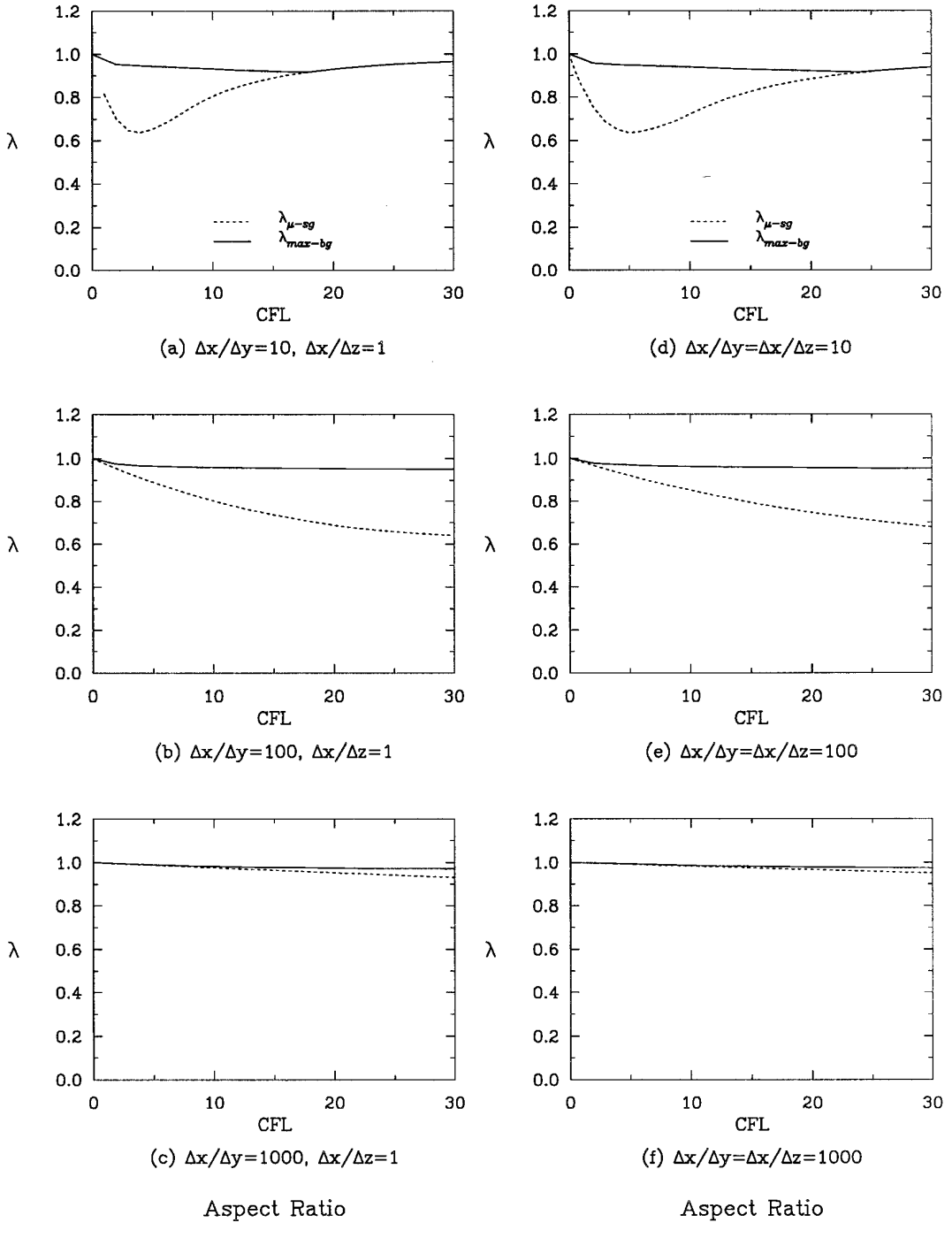

FIG. 18. 3-D Navier–Stokes equations using central schemes: (a)–(f) convergence characteristics—aspect ratio (Re = 100, $\varepsilon_e = 0.5$, $\varepsilon_i = 1.0$, $\nu^1 = 1$, $\nu^2 = 0$).

APPENDIX A. THE BI-GRID AMPLIFICATION MATRIX $\hat{M}(\Theta)$

$$\hat{M}(\Theta) = \begin{bmatrix} M_{11} & M_{12} & M_{13} & M_{14} & M_{15} & M_{16} & M_{17} & M_{18} \\ M_{21} & M_{22} & M_{23} & M_{24} & M_{25} & M_{26} & M_{27} & M_{28} \\ M_{31} & M_{32} & M_{33} & M_{34} & M_{35} & M_{36} & M_{37} & M_{38} \\ M_{41} & M_{42} & M_{43} & M_{44} & M_{45} & M_{46} & M_{47} & M_{48} \\ M_{51} & M_{52} & M_{53} & M_{54} & M_{55} & M_{56} & M_{57} & M_{58} \\ M_{61} & M_{62} & M_{63} & M_{64} & M_{65} & M_{66} & M_{67} & M_{68} \\ M_{71} & M_{72} & M_{73} & M_{74} & M_{75} & M_{76} & M_{77} & M_{78} \\ M_{81} & M_{82} & M_{83} & M_{84} & M_{85} & M_{86} & M_{87} & M_{88} \end{bmatrix}.$$

The diagonal elements are

$$\begin{aligned} M_{11} &= \mathbf{I} - \hat{I}_H^h(\Theta^1)\hat{I}_h^H(\Theta^1)\hat{L}_h(\Theta^1)\hat{S}_1^{\nu_1}(\Theta^1)\hat{S}_2^{\nu_2}(\Theta^1)\hat{L}_H^{-1} \\ M_{22} &= \mathbf{I} - \hat{I}_H^h(\Theta^2)\hat{I}_h^H(\Theta^2)\hat{L}_h(\Theta^2)\hat{S}_1^{\nu_1}(\Theta^2)\hat{S}_2^{\nu_2}(\Theta^2)\hat{L}_H^{-1} \\ M_{33} &= \mathbf{I} - \hat{I}_H^h(\Theta^3)\hat{I}_h^H(\Theta^3)\hat{L}_h(\Theta^3)\hat{S}_1^{\nu_1}(\Theta^3)\hat{S}_2^{\nu_2}(\Theta^3)\hat{L}_H^{-1} \\ &\vdots \\ M_{33} &= \mathbf{I} - \hat{I}_H^h(\Theta^8)\hat{I}_h^H(\Theta^8)\hat{L}_h(\Theta^8)\hat{S}_1^{\nu_1}(\Theta^8)\hat{S}_2^{\nu_2}(\Theta^8)\hat{L}_H^{-1} \end{aligned}$$

and the off-diagonal elements are

$$M_{nm} = -\hat{I}_H^h(\Theta^n)\hat{I}_h^H(\Theta^m)\hat{L}_h(\Theta^m)\hat{S}_1^{\nu_1}(\Theta^n)\hat{S}_2^{\nu_2}(\Theta^m)\hat{L}_H^{-1},$$

where, for example,

$$\begin{aligned} M_{21} &= -\hat{I}_H^h(\Theta^2)\hat{I}_h^H(\Theta^1)\hat{L}_h(\Theta^1)\hat{S}_1^{\nu_1}(\Theta^2)\hat{S}_2^{\nu_2}(\Theta^1)\hat{L}_H^{-1} \\ M_{32} &= -\hat{I}_H^h(\Theta^3)\hat{I}_h^H(\Theta^2)\hat{L}_h(\Theta^2)\hat{S}_1^{\nu_1}(\Theta^3)\hat{S}_2^{\nu_2}(\Theta^2)\hat{L}_H^{-1} \\ M_{84} &= -\hat{I}_H^h(\Theta^8)\hat{I}_h^H(\Theta^4)\hat{L}_h(\Theta^4)\hat{S}_1^{\nu_1}(\Theta^8)\hat{S}_2^{\nu_2}(\Theta^4)\hat{L}_H^{-1} \\ M_{76} &= -\hat{I}_H^h(\Theta^7)\hat{I}_h^H(\Theta^6)\hat{L}_h(\Theta^6)\hat{S}_1^{\nu_1}(\Theta^7)\hat{S}_2^{\nu_2}(\Theta^6)\hat{L}_H^{-1} \end{aligned}$$

Each element is a 5×5 matrix corresponding to the five dependent variables in Eq. (31).

ACKNOWLEDGMENT

This work was funded by the NASA Lewis Research Center under Grant No. NAG-3-1329 with Dr. James Scott as Technical Monitor. Computations were performed on supercomputers at NASA Lewis and NASA Ames Research Centers. We are grateful to Dr. Eric Morano of ICASE, NASA Langley Research Center, for his advice and suggestions.

REFERENCES

1. R. P. Federenko, *Z. Vycisl. Mat. Mat. Fiz.* **1,** 922 (1961).
2. R. P. Federenko, *Z. Vycisl. Mat. Mat. Fiz.* **4,** 559 (1964).
3. N. S. Bakhalov, *Z. Vycisl. Mat. Mat. Fiz.* **6,** 861 (1966).
4. K. Stuben and U. Trottenberg, Multigrid methods: Fundamental algorithms, model problems analysis and applications, in *Multigrid Methods,* Lecture notes in Mathematics, Vol. 960 (Springer-Verlag, New York, 1982), p. 1.
5. W. Hackbusch, *Ein iteratives verfahren zur schnellen Auflosung elliptisher Randevertprobleme,* Report 76-12, Institut fur Angewandte Mathematika, (Universitat Koln, 1976).
6. A. Brandt, *Math. Comput.* **31,** 138 (1977).
7. A. Brandt, *Rigorous Quantitative Analysis of Multigrid,* Preliminary Report Prepared for Air Force Office of Scientific Research, (United States Air Force, 1991).
8. E. J. van Asselt, The multigrid method and artificial viscosity, in *Multigrid Methods* Lecture Notes in Mathematics, Vol. 960 (Springer-Verlag, New York, 1982), p. 313.
9. W. A. Mulder, Analysis of a multigrid method for the Euler equations of gas dynamics in two dimensions. in *Multigrid Methods, Theory, Applications and Supercomputing,* Lecture Notes in Pure and Applied Mathematics, edited by S. F. McCormick, (Dekker, New York, 1988), p. 467.
10. W. A. Mulder, *J. Comput. Phys.* **83,** 303 (1989).
11. G. Horton and S. Vandewalle, submitted for publication.
12. A. Brandt and I. Yavneh, *SIAM J. Sci. Comput.* **14,** 607 (1993).
13. E. Morano, *Resolution des equations d'Euler par une methode multigrille stationaire,* Ph.D. Thesis (University de Nice Sophia-Antipolis, 1992), p. 50.
14. E. Morano and A. Dervieux, submitted for publication.
15. S. O. Ibraheem and A. O. Demuren, Bi-grid stability analysis method for multigrid prediction in Burger's equation. in *Proceedings, SIAM 18th Annual Meeting, Southeastern-Atlantic Section, Winston-Salem, North Carolina, March 1994,* p. 20.
16. A. Jameson and S. Yoon, *Multigrid Solution of the Euler Equations Using Implicit Schemes,* AIAA Paper 85-0293 (1985).
17. D. A. Caughey, *AIAA J.* **26,** 841 (1988).
18. W. K. Anderson, J. L. Thomas, and D. L. Whitfield, *Three-Dimensional Multigrid Algorithms for the Flux-Split Euler Equations,* NASA TP-2829 (1988).
19. A. O. Demuren and S. O. Ibraheem, *Numer. Heat Transfer B* **25,** 97 (1994); also NASA TM-106314 (1993).
20. A. Jameson, W. Schmidt, and E. Turkel, *Numerical Solutions of the Euler Equations by Finite Volume Methods Using Runge–Kutta Time-Stepping Schemes,* AIAA Paper 81–1259 (1981).
21. R. M. Beam and R. F. Warming, *AIAA J.* **16,** 393 (1978).
22. D. A. Anderson, J. C. Tannehill, and R. H. Pletcher, *Computational Fluid Mechanics and Heat Transfer* (McGraw–Hill, New York, 1984), p. 489.
23. J. L. Steger and R. F. Warming, *J. Comput. Phys.* **40,** 263 (1980).
24. B. van Leer, *Flux-Vector Splitting for the Euler Equations,* ICASE 82-30 (1982).
25. A. Jameson and E. Turkel, *Math. Comput.* **37,** 385 (1981).
26. A. O. Demuren and S. O. Ibraheem, *Convergence Acceleration of the Proteus Computer Code with Multigrid Methods,* Interim Report Prepared for the Internal Fluid Mechanics Division, NASA Lewis Research Center, (1992).
27. C. E. Towne, J. R. Schwab, T. J. Benson, and A. Suresh, *PROTEUS Two-Dimensional Navier–Stokes Computer Code—Version 1.0, Volumes 1–3,* NASA TM's-102551-3 (1990).